Terahertz nondestructive evaluation of additively manufactured and multilayered structures

Alexander T Clark, Jessy Nemati, Christopher Bolton, Nickolas Warholak, Jimmie Adriazola, Ian Gatley, Samuel Gatley, and John F Federici, Department of Physics, New Jersey Institute of Technology, Newark, NJ, United States

Abstract

A major barrier in the adaptation of additive manufacturing into the realm of accepted manufacturing technologies is the requirement for rapid and standardized approaches for qualification of materials and processes. Terahertz nondestructive evaluation techniques could play a major role in the creation of a standardized qualification process for additively manufactured components. This chapter showcases the current use of terahertz nondestructive evaluation on two emerging material applications: additively manufactured components and multilayer paint stacks.

Key points

- Terahertz nondestructive evaluation techniques could play a major role in the creation of a standardized qualification process for additively manufactured components.
- The current use of terahertz nondestructive evaluation on two emerging material applications are showcased: additively manufactured components and multilayer paint stacks.
- As new materials for additive manufacturing are developed and new printing techniques are created, standardized approaches for rapid qualification of these materials and processes will be required.
- Owing to refractive effects, terahertz nondestructive evaluation is best suited to planar structures. Examples include the material characterization and thickness measurements of multilayer paint stacks.
- Based on the accelerated corrosion studies using salt-fog exposure and humidity cycling, a 5.6% change in the reflectivity from the metallic layer indicates significant chemical corrosion of the multilayer paint coating prior to any visible evidence of a blister on the coating surface. Further chemical corrosion (and commensurate decrease in terahertz reflectivity) leads to detachment of the coating from the substrate.
- The major driving force behind the development of additively manufactured terahertz and microwave components is the development of next-generation wireless communication systems.

- Various terahertz quasi-optical devices including GRIN lenses, topological waveplates, phase plates, polarization splitters, q-plates, and stepped-refractive-index lenses have been fabricated by 3D printing.
- Terahertz imaging can detect defects in additively manufactured structures which could significantly impact their functionality.
- Terahertz computed tomography of additively manufactured parts has many of the same analysis capabilities as X-ray computed tomography: detection of internal voids and defects, measure internal and external geometry, and ability to compare printed parts to their computer-aided design.
- Corrections to terahertz computed tomography analysis to account for Gaussian beam propagation as well as refractive effects have been demonstrated.

Introduction

Terahertz nondestructive evaluation

Terahertz (THz) radiation refers to the range of electromagnetic waves between the microwave and infrared from 0.1 to 10 THz and wavelengths of 3 mm–30 μm (Wang and Zhang, 2004). Technology related to the creation, manipulation, and implementation of these waves within the "THz gap" is still relatively new and not widely utilized. Since THz waves are nondestructive and do not carry enough energy per quantum to ionize the atoms or molecules that are exposed to them, THz radiation offers many benefits over other traditional material evaluation techniques. These frequencies can be used for spectroscopy, imaging, and structural evaluation. There are many ways to generate and detect THz waves. THz systems can employ either continuous wave or pulsed wave configurations. The most common continuous wave systems use photomixing for tunable narrowband generation while pulse-based systems generate a broadband pulse using biased photoconducting antennas (PCA) (Mittleman, 2003).

Nondestructive evaluation (NDE) methods test and inspect various aspects and characteristics of materials, components, and full systems without permanent damage. NDE is extremely useful in various fields of research and industry because it can save time and money by allowing for rapid, successive, and significant assessment without sacrificing the object being inspected. Valuable or rare samples can be spared where other evaluation techniques might damage them (Sathishkumar et al., 2020).

This chapter describes the use of THz spectroscopy and imaging for NDE on two emerging material applications: additively manufactured components and multilayer paint stacks. For the first application, NDE of fused deposition modeling (FDM) printed plastics and nanoparticle jetted ceramics are emphasized. For the second application, NDE is used to determine both the frequency-dependent permittivity and thicknesses of individual paint layers, while also evaluating corrosion which is hidden below the outer paint surface.

Additive manufacturing—Plastics and ceramics

The terms additive manufacturing (AM) and three-dimensional (3D) printing can generally be used interchangeably: they encompass all the processes that create objects or structures by adding material as opposed to removing it in subtractive manufacturing. There are currently seven common types of additive manufacturing: material extrusion, sheet lamination, vat polymerization, powder bed fusion, material jetting, binder jetting, and direct energy deposition (Alfattni, 2022). The specific process chosen depends on the application's needs. Despite its popularity and promise, AM is currently being held back from becoming a mainstream manufacturing technique by the lack of standards for quality assurance and qualification of the AM parts. Many industries have expressed concern about this lack of standardization, and The National Institute of Standards and Technology (NIST) reports that there are presently no additive manufactured materials or processes that have been specifically qualified for aerospace or critical defense applications (Moylan, n.d.).

In 2021, the United States Department of Defense (DoD) released an updated version of an AM roadmap, originally created in 2016 with *America Makes*, outlining the current objectives of AM and the barriers that must be overcome. Specifically, this roadmap lays out the steps needed to mature the technology of AM in order both for the DoD to fully adopt and utilize this technology, and to allow applications in the public sector. In this current strategy, the DoD identifies the number one barrier to moving AM into the realm of accepted manufacturing technologies as "rapid and standardized approaches for qualification of materials and processes, and certification of AM parts." Yet, as stated in the original DoD roadmap, additive manufacturing has the ability to become cheaper, faster, and more reliable than most current manufacturing techniques (Fielding et al., 2021). The development of THz NDE techniques for these AM parts can play a major role in the full adoption of this technology through the creation of a standardized qualification process (Joint Defense Manufacturing Council, 2021).

The term "qualification" refers to the fulfillment of requirements in the original design: for example, the final product must satisfy dimension constraints, and a major concern with additively manufactured parts is post-printing material shrinkage. An application example that requires strict dimensional constraints is dental crowns, where research has been performed on creating low shrinkage ratio materials; but even those optimized AM materials show signs of shrinkage of over 2% (Zhao et al., 2021).

In a wide variety of applications, for a product to be functional, evaluation and qualification of its final dimensions is crucial. AM parts frequently have structural defects and internal voids caused by the printing process that are not seen under inspection because the part is not transparent to visible light; but in such circumstances, THz NDE can allow defect detection through non-contact imaging.

THz spectroscopy can also characterize the electromagnetic properties of AM structures and has been proven to be a reliable means for optical property characterization (Yasuda and Hosako, 2008; Yilmaz and Akan, 2020; Waddie et al., 2020; Ruan and Chan, 2019). Recently, there have been advances in using FDM printers to print microwave and THz-based passive optical components including waveplates, phase plates, antennas, and lenses (Rohrbach et al., 2021; Zhang et al., 2017; Siemion et al., 2020). AM ceramic structures have been designed for applications in capacitors, filters, dielectric resonator antennas, and 5G devices (Goulas et al., 2020; Morales et al., 2021). The accuracy, reproducibility, and electromagnetic response of such AM structures will likely depend on the structures' printing parameters, and so the ability to tune properties such as refractive index, attenuation coefficient, birefringence, and relative permittivity will be important. Utilization of THz NDE for printed optical components and their material characteristics will be discussed later in this chapter.

Terahertz NDE is well-suited for the characterization of planar structures, where refractive effects due to curved surfaces are minimized. Moreover, using broad-banded terahertz pulses with time durations in the few picoseconds range results in high spatial resolution in the direction of the pulse propagation (a typical resolution is about 10 μm, which is much smaller than the wavelength of the terahertz radiation). In the transverse direction, the spatial resolution of freely propagating terahertz radiation is limited by Gaussian beam propagation and diffraction to several electromagnetic wavelengths.

THz computed tomography (CT) can be used to create 3D reconstructions of a structure being imaged. Like traditional X-ray CT, THz CT has been implemented for NDE internal structure observation; previous research includes the comparison and evaluation of various reconstruction algorithms using THz CT (Recur et al., 2011). But to date, little research has been done utilizing THz CT on 3D printed structures, although various correction algorithms have been created to correct for refraction losses and Fresnel reflection boundary effects observed when utilizing THz for CT (Abraham et al., 2010; Mukherjee et al., 2013). If implemented, THz CT of AM structures could be useful in rapid prototyping, failure analysis, and material characterization.

THz NDE of multilayer paint stacks

An important example of THz NDE of planar structures is the study of multilayer paint systems. Terahertz waves can penetrate many non-conductive materials, enabling a contactless testing method. In such studies, terahertz time-domain reflection measurements are sometimes referred to as terahertz pulse imaging (TPI). In its simplest form, the THz-TD transmitter emits a near-single cycle electromagnetic pulse with a bandwidth from ∼0.1 to 3 THz. This extremely wide bandwidth pulse is focused on the coating, and echo pulses are generated from each interface (air-layer, layer-layer, layer-substrate). The terahertz radiation penetrates the whole coating stack and samples the properties of each layer provided that the layer is not metallic. By analyzing the reflected THz pulse, one can reconstruct the thicknesses as well as the permittivity ε and permeability μ of each paint layer. Equivalently, one can characterize the properties of each layer through its complex refractive index $\tilde{n} = \sqrt{\varepsilon\mu/\varepsilon_o\mu_o}$ where $\varepsilon/\varepsilon_o$ and μ/μ_o are the permittivity and magnetic permeability of the paint layer relative to a vacuum.

Over the last 15 years, terahertz nondestructive evaluation and imaging has found application to various multilayer coating structures (paints and ceramic coatings) for several industries including aerospace and automotive (Krimi et al., 2016; Krimi et al., 2017; Catapano et al., 2017; Bohn and Petkie, 2013; Su et al., 2014; Ellrich et al., 2020; Stoik et al., 2008; Yasuda et al., 2007; Su et al., 2014). More specifically, it has been used as a method for the testing of dried paint layers on automotive vehicles for quality control as well as determining the thickness of the paint layers (Takeshi Yasui et al., 2005; Yasuda et al., 2006; Federici, 2012; Yasuda et al., 2007; Su et al., 2014; Krimi et al., 2016). As pointed out by Krimi et al. (2017) materials for coatings and substrates are continuously improved requiring concomitant improvements in quality control and thickness monitoring technologies. Examples of substrate innovations over standard metals include carbon fiber-reinforced polymers and glass fiber-reinforced polymers. In many cases, the substrate materials are highly reflective, thus requiring that terahertz NDE be performed in a reflective mode. Terahertz techniques are effective not only for measuring the frequency-dependent permittivity and thicknesses of the various layers but also for detecting the presence of defects.

Additive manufacturing

This section mainly focuses on the use of FDM printing and nanoparticle jetting for AM, but all AM follows a general order-of-procedures to 3D print an object. First, a 3D model of the structure is created using Computer-Aided Design (CAD) software. The model is then transferred to slicing software, where the different structural parameters are chosen. The structure's infill, layer heights, size, orientation, and other parameters can be altered. The slicing software then converts the model into a programming language called G-code which commands the printer to print the model (Evans, 2012) in a hands-off process to complete the part. Once an object or sample has been printed, THz NDE can be employed.

The major driving force behind the development of additively manufactured terahertz and microwave components is the development of next-generation wireless communication systems (Federici et al., 2016; Federici et al., 2013; Federici and Moeller, 2010). Since these additively manufactured components are designed specifically to focus, split, and otherwise manipulate terahertz radiation, it is critical to characterize the refractive index, attenuation, and birefringence of the component materials in the terahertz frequency range. Aside from terahertz optical components, THz NDE is important for material characterization of additively manufactured materials—such as polymers, ceramics, and composites. Using THz NDE, images of the structure can be taken, optical properties of the materials can be characterized, defects in the structures can be discovered, 3D computed tomography models can be created, residual stresses in the structures can be mapped, etc. Generally speaking, the end goal is to qualify the additively manufactured part—does it function (physical dimensions, mechanical stress, porosity, etc.)—as designed?

THz spectral characterization of materials

THz NDE has the capability to characterize different optical properties of materials. Analysis of the THz waves can be implemented in the time-domain, for example, by measuring the time delay of a waveform or in the frequency domain via the Fourier transform of the time versus THz electric field measurements (Mittleman, 2003). By taking the discrete Fourier transform (DFT) of measured voltages, using a Fast Fourier Transform (FFT) algorithm, the time domain data can be represented in the frequency domain for analysis. Using frequency domain data, the complex refractive index, transmission coefficient, attenuation coefficient, relative permittivity, and birefringence of THz transparent materials can all be measured. For calculation of the complex refractive index of a material, while considering the sample's thickness, three THz waveforms are required: an averaged sample waveform, a reference waveform, and a background waveform. The reference waveform usually consists of the measured time-domain waveform with either the sample removed (for a transmission geometry) or the sample replaced by a perfect mirror (for a reflection geometry). The background waveform corresponds to a measured offset in the time-domain waveform which is recorded when the THz beam is blocked. Subtracting the background waveform from the sample waveform removes the offset.

The time-domain waveform data is converted to the frequency domain via a Fourier transform to calculate both the real and imaginary parts of the refractive index as a function of frequency. The phase angles as a function of frequency are calculated for both the averaged sample and reference waveforms and are used to calculate the frequency-dependent real refractive index $n_r(v)$ using the relationship

$$n_r(v) = 1 + \frac{c_o \, \Delta\phi(v)}{2\pi L v} \tag{1}$$

where c_o is the speed of light, $\Delta\phi(v)$ is the frequency-dependent phase difference between the sample and reference waveforms, L is the thickness of the sample measured, and v is the frequency. Once the frequency-dependent real refractive index is calculated, it is possible to select a specific frequency at which to compare the real refractive indices.

Since most non-conductive plastic samples are relatively transparent in the THz frequency range, the imaginary refractive index is small compared to the real refractive index. The measured amplitude of the transmitted THz Fourier transform can be corrected for Fresnel reflection losses at the air-sample and sample-air interfaces (Prabhu, 2018). Using the real refractive index to correct for losses at the boundary, the imaginary refractive index can be calculated using

$$n_i(v) = \frac{c_o}{2\pi v L} \ln\left(\frac{|E_R(v)|}{|E_S(v)|} t_{12} t_{21}\right) \tag{2}$$

where $|E_R(v)|$ and where $|E_S(v)|$ represent the magnitudes of the DFT of the electric field measurements of the reference and sample waveforms, respectively. The Fresnel transmission coefficients at normal incidence between air and the sample and the sample and air are represented by t_{12} and t_{21} and are calculated using

$$t_{12}(v) = 2/(1 + n_r(v)) \tag{3}$$

and

$$t_{21}(v) = 2 n_r(v)/(n_r(v) + 1). \tag{4}$$

The attenuation coefficient can be calculated using the resulting corrected imaginary refractive index by

$$\alpha = 2\pi v n_i/c_o. \tag{5}$$

The frequency-dependent refractive indices and attenuation coefficients for many common 3D printable plastics have been previously characterized (Castro-Camus et al., 2020; Clark et al., 2021).

Additively manufactured THz optical components

Using the THz spectral measurements in combination with AM, recent studies have shown that it is possible to create operable microwave and THz optical components. One of the technical applications driving the push to develop low-cost terahertz and sub-terahertz components is the shift of wireless communications from the currently used few GHz bands to higher carrier
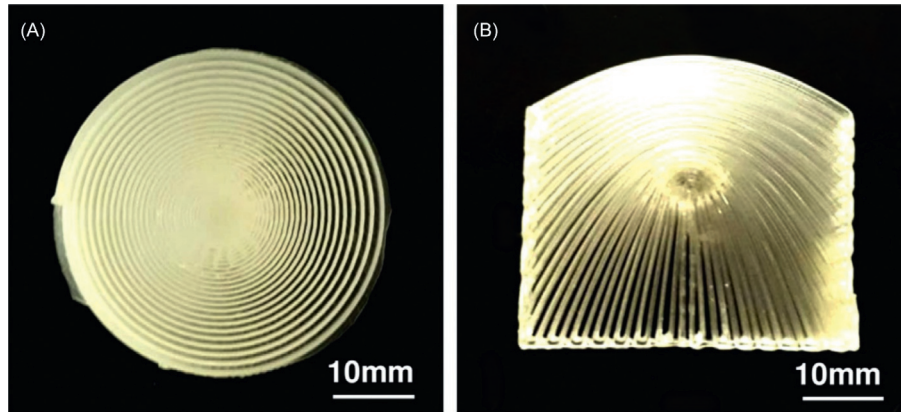
Fig. 1 Examples of 3D printed terahertz components. (a) A Gradient-Refractive-Index (GRIN) lens (b) topological waveplate. From Castro-Camus E, Koch M and Hernandez-Serrano AI (2020) Additive manufacture of photonic components for the terahertz band. *Journal of Applied Physics* **127**: 210901.

frequencies in the several hundreds of GHz band (Federici et al., 2016; Federici et al., 2013; Federici and Moeller, 2010). Several research teams have succeeded in creating various THz quasi-optical devices fabricated by 3D printing. Fig. 1 shows examples of a 3D printed gradient-index (GRIN) lens as well as a topological waveplate. Because the resulting refractive index and birefringence of these materials could be measured using THz NDE, it was possible to tailor these lenses for specific applications (Castro-Camus et al., 2020). As another example, Fig. 2 shows experimental nylon polyamide (PA6) diffractive lenses and their resulting irradiance measured at the plane of the lens—another successful implementation of using FDM for the creating of THz-based optical components (Furlan et al., 2016). Many other THz optical components (including phase plates (Rohrbach et al., 2021), polarization splitters, q-plates, and stepped-refractive-index lenses (Serrano, 2018)) have also been created using AM for the terahertz frequency range.

The AM fabrication process of terahertz optical components presently suffers several limitations. Currently, there are only a limited number of materials that are usable within FDM 3D printers, and even fewer whose transparency is within a usable range (Castro-Camus et al., 2020). For example, polylactic acid (PLA) is a common 3D printed plastic, but unfortunately, it exhibits a high absorption in the terahertz frequency range. Consequently, unless the material is very thin, it will not transmit sufficient terahertz radiation to be functional. Some of the currently used polymers for the manufacturing of terahertz optical components include high-density polyethylene (HDPE), polypropylene, polystyrene, TOPAS (also known as cyclic olefin copolymer (COC)). Most of these polymers exhibit relatively minimal attenuation, but also have refractive indices close to 1.5. A consequence of this similarity of refractive indices is that certain optical components, such as photonic crystals with large bandgaps (where a significant refractive index contrast is required), are very challenging to print.

Another limitation of current economically viable FDM 3D printers is their relatively poor resolution. Since the resolution of these printers is still relatively coarse, the resulting printed optical components must operate within the low range of a few hundred gigahertz, the low end of the THz band. Other types of AM such as stereolithography (SLA) resin printers can produce higher resolution prints, but generally they are much more expensive, and the compositions of the materials may be proprietary. Yet, as FMD technology progresses and evolves, more polymers will be adapted, and the resolution will improve, allowing for increased quality in optical component fabrication (Castro-Camus et al., 2020).

THz NDE of additively manufactured components

In this section, several THz NDE modalities for characterizing additively manufactured components are described. The modalities focus on key aspects of component specification:

- THz for infill structures—Internal infill structure and infill percentage are major considerations for the structural and mechanical strength of 3D printed components.
- THz imaging for defect detection—Defects in the 3D printed structures could significantly impact their functionality. Simple examples include cracks/ voids in the printed structure or regions of high mechanical stress.
- Effect of print parameters on THz properties—3D printing parameters can have an effect on the resulting optical properties of the final printed structure. The ability to fine-tune the optical properties of these structures including refractive index, attenuation coefficient, and birefringence is crucial to the design and fabrication of various optical components.
- THz CT—A complete 3D image of an AM part could enable a detailed comparison of design versus printed dimensions, structural defects, etc. THz CT of AM parts has many of the same analysis capabilities as X-ray CT: detection of internal voids and defects, measure internal and external geometry, and ability to compare printed parts to their CAD design. However, THz CT
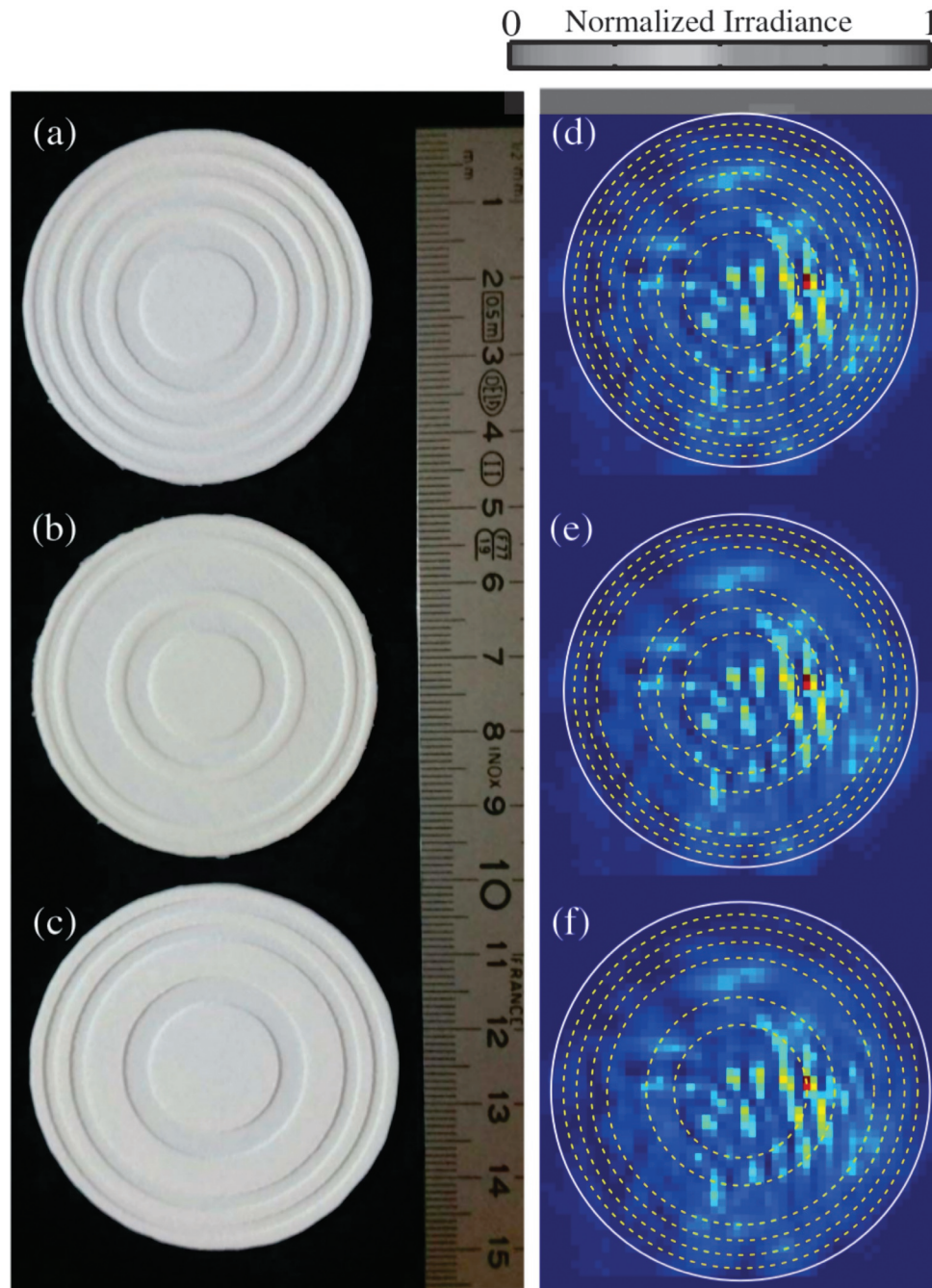
Fig. 2 Examples of 3D printed THz diffractive lenses. (a) Fresnel, (b) fractal, and (c) Fibonacci models. The corresponding maps of THz irradiance measured at the plane of the lens are shown in the second column of images. Reprinted with permission from Furlan WD, Ferrando V, Monsoriu JA, Zagrajek P, Czerwińska E and Szustakowski M (2016) 3D printed diffractive terahertz lenses. *Optics Letters* **41**: 1748–1751.© The Optical Society.

exhibits some challenges as well as advantages when compared to X-ray CT. Challenges include correcting for refraction of THz rays, Gaussian beam profiles, and more limited spatial resolution. However, THz enables an additional modality which X-Ray CT does not: visualization of stress/strain in the printed part through the photoelastic effect.

- THz birefringence—Clearly, characterizing the birefringence of additively manufactured materials is an important parameter for 3D printed terahertz components. The birefringence, typically manifested through a photoelastic effect—can be either intrinsic due to residual internal stress within the material or induced via an externally applied stress. For some components, such as additively manufactured lenses, one would typically require minimal birefringence. For other components such as those whose functionality is dependent upon the phase delay of propagating terahertz waves, the ability to fabricate structures with a controllable birefringence might be important.

THz NDE of infill structures

Key structural and mechanical strength considerations of 3D printed structures are the internal infill structure and infill percentage. Terahertz time-domain imaging of 3D printed infill structures (Busboom et al., 2021) shows that THz NDE can be used to visualize the infill structures. Useful imaging modalities include both transmitted power in a frequency band as well as pulse time-of-flight measurements. Transmission measurements are easier to implement, but are limited if the material is too thick (ABS which was used in (Busboom et al., 2021) to fabricate the structures exhibits a large absorption in the terahertz range) or the infill structure is too complex. Reflection measurements are useful to determine which grid direction is printed first enabling a clearing visualization of the infill structure. While these results are interesting, the samples under study were oriented such that the walls of the infill were always perpendicular to the propagating terahertz beam direction. An arbitrary orientation of the infill structure relative to the beam direction would require a computed tomography modality to render a 3D image of the infill structure.

THz imaging of defects

As an example of defect imaging, NDE of ceramic samples is presented (Clark et al., 2021) in this section. The samples were fabricated using an XJet Carmel 1400 nanoparticle jet printer. Nanoparticle jetting is a proprietary printing technology developed by XJet, which falls under the category of binder jetting additive manufacturing. ZrO_2 nanoparticles are suspended in a polymer binder and carrier agent to form an ink. As multiple print nozzles deposit layers of the ZrO_2 dispersion on top of one another, as well as support structure material, the carrier agent is evaporated and the layers are dried using heat lamps and hot air dryers. The support material is dissolved from the print by submerging the structure in water. After a period of drying in a desiccating chamber, the samples are ready for sintering. Processing above 1200 °C is required to convert the mixture of monoclinic and tetragonal phases into a mixture of tetragonal and cubic phases and join the individual ZrO_2 particles into a dense ceramic structure. Voids form as the polymer binder decomposes, where the size, shape, and distribution of these defects depend upon the maximum firing temperature. The samples used in this example were all printed with identical printing parameters, but experienced different maximum firing temperatures varying from 750 °C to 1450 °C in increments of 100 °C. The samples were 50 mm^2, 2–3 mm thick, with printed layer thicknesses of 10 μm, and a jetting resolution of roughly 20 μm.

The relative permittivity of the extruded ceramics was measured by mounting the samples to an XY gantry away from the focal point of the lens. This was done to create a larger spot size interacting with the samples in a transmission configuration. The samples are measured between 60 GHz and 3 THz using the T-ray 5000 system using an average of 2000 acquired THz waveforms. Valid data is extracted between 110 GHz and 550 GHz due to the low signal-to-noise ratio. To show and verify that this data is accurate and repeatable, the samples are also measured between 75 GHz and 110 GHz using a free-space focused beam system.

The data in Fig. 3 from the free-space system matches the T-ray 5000 data very well, confirming that these are accurate measurements. This data confirms that as a product of increased firing temperature, the relative permittivity increases, while not
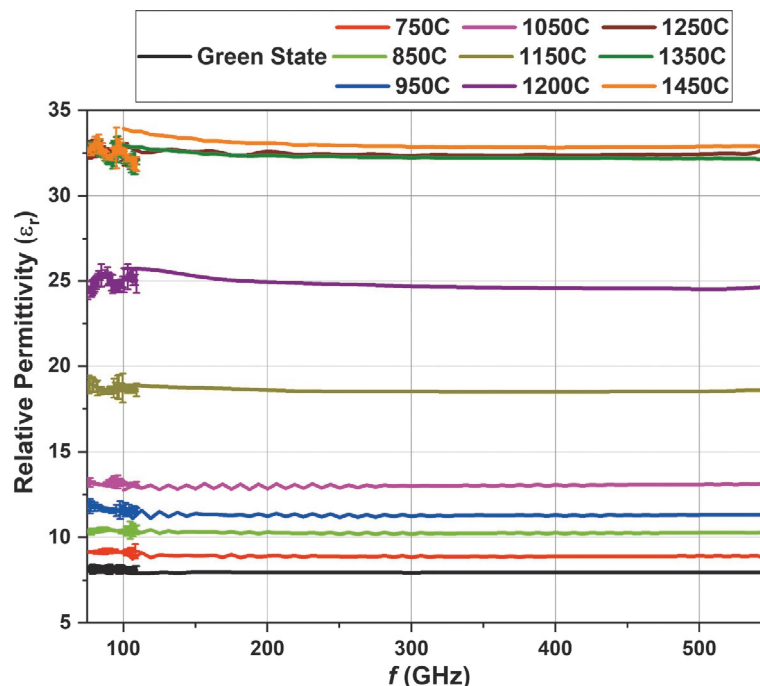

Fig. 3 Relative permittivity of the various sintered ceramic samples at different sintering temperatures showing data between 75 GHz and 550 GHz provided by Paul Parsons. "Green State" refers to an un-sintered sample. From Clark AT (2022) *Nondestructive Evaluation of 3D Printed, Extruded and Natural Polymer Structures using Terahertz Spectroscopy and Imaging*. Ph.D. Doctoral Dissertation, New Jersey Institute of Technology.

varying over a relatively large frequency range. At temperatures above 1200 °C, where the structure conversion takes place, the relative permittivity reached a value where the increase between samples decreased dramatically, almost to zero.

Small location-dependent variations in the relative permittivity were observed when the THz beam was focused over a small spot size on the sample. Images were taken by raster scanning the samples in a transmission configuration to investigate these variations. The contrast of the images shows the variations in the dielectric constant of the material at each pixel. As the particles begin to sinter, and voids begin to disappear with increasing temperature, all the samples show clear isotropic volume reduction. The samples decrease in volume from 1% up to 18% at the highest sintering temperature of 1450 °C. There are also numerous horizontal striations seen in all the samples. An alignment issue with the XJet printer, verified by Xjet staff, was the cause of these striations, resulting in a major flaw throughout each of the prints. The flaws shown in Fig. 4, a consequence of misaligned print heads, are effectively an inhomogeneity in the dispersion of the ZrO_2 particles.

In the 1450 °C sample, a dark wavy horizontal feature about one-third of the way down is visible, marked by the white arrow. This is a crack that runs throughout the entire length of the sample. A combination of material shrinkage and inhomogeneous particle density caused by the misaligned print heads is to blame. More importantly, this crack is not fully visible under visual inspection. With post THz imaging, only then the full extent of the crack was observed. This is a clear and successful application of using THz NDE for both electromagnetic property characterization as well as the detection of defects within AM ceramic structures.

Effect of 3D printing parameters on FDM printed components

When printing optical components such as the GRIN lens or diffractive lenses shown in Figs. 1 and 2, it is important to know if the printing parameters will have any effect on the resulting optical properties of the final structure. When any structure is printed, there are multiple different parameters that are either automatically chosen by the slicing software or manually picked by the user. The ability to fine-tune the optical properties of these structures including refractive index, attenuation coefficient, and birefringence will rest on detailed knowledge of such dependencies (Alfattni, 2022). Commonly altered printing parameters include the printer's nozzle size, the layer height within the print, or a print's orientation. For example, if the refractive index of a 3D printed terahertz lens varies with printing parameters, then the focal length of the lens would be dependent on printing parameters. Likewise, if the attenuation depended on printing parameters, then the throughput transmission of the lens would be dependent on the printing parameters as well. Similarly, if the refractive index, attenuation coefficient, or birefringence of a printed THz waveguide were to vary due to printing parameters, then the device performance (e.g. propagation speed of guided terahertz, numerical aperture of the waveguide, loss per unit length of the waveguide) would all be dependent on the various printing parameters.

Refractive index, attenuation coefficient, and level of birefringence have been measured for a set of 3D printed samples printed with various printing parameters (Clark et al., 2021). The samples were rectangular blocks of various clear filaments printed using a commercial 3D printer. Changes in the optical properties of these printed structures are observed and compared. The THz optical properties of the materials studied here have previously been demonstrated to be frequency-dependent. Optical property changes have been isolated at 500 GHz. At this frequency, there is a good signal-to-noise ratio and lack of interference oscillations in the measured data.

Table 1 shows the variation based on changing the print orientation of the structure. The print orientation dictates whether the rectangular block sample was printed either laying down (horizontal) or up on edge (vertical). By changing the print orientation, the planes in which individual layers are printed are altered. There is a clear correlation between print orientation and change in refractive index: an average increase of 1.9% in the real refractive index at 500 GHz when the samples are printed horizontally compared to vertically. Three of the four measurable attenuation coefficients have increases greater than the calculated uncertainty.
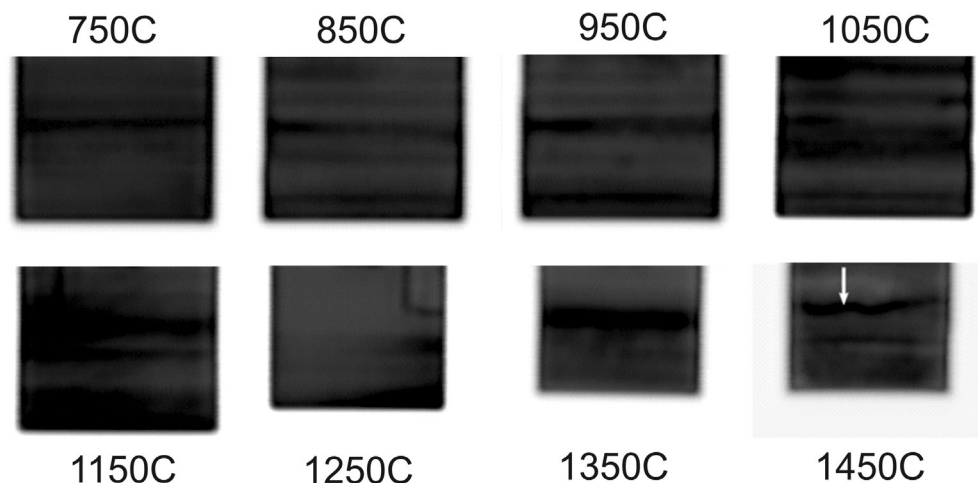

Fig. 4   Raster scan images of the dielectric constants of varying sintering temperature ZrO_2 samples. Horizontal striations seen throughout are a result of print head misalignment during the printing process. A crack in the 1450 °C is indicated by the white arrow. From Clark AT (2022) *Nondestructive Evaluation of 3D Printed, Extruded and Natural Polymer Structures using Terahertz Spectroscopy and Imaging*. Ph.D. Doctoral Dissertation, New Jersey Institute of Technology.

Table 1   Real refractive indices and attenuation coefficients of samples at 500 GHz based on variation in print orientation (Clark et al., 2021).

Filament Material	Print Orientation	Real Refractive Index (n)	Attenuation Coefficient (cm^{-1})
PLA	Horizontal	1.654	4.429
	Vertical	1.604	5.092
Nylon	Horizontal	1.749	4.015
	Vertical	1.741	4.099
PC	Horizontal	1.649	1.944
	Vertical	1.623	2.444
CPE	Horizontal	1.683	3.343
	Vertical	1.650	3.191
PP	Horizontal	1.492	N/A
	Vertical	1.457	N/A

Note: Standard printing parameters of a 0.4 mm nozzle and 0.2 mm layer heights were used. Uncertainties in the real refractive index: $2\sigma = \pm 0.010$ and attenuation coefficient: $2\sigma = \pm 0.025$.
From Clark AT, Federici JF and Gatley I (2021) Effect of 3D printing parameters on the refractive index, attenuation coefficient, and birefringence of plastics in terahertz range. *Advances in Materials Science and Engineering* **2021**: 8276378.

Fig. 5   Level of birefringence ($\frac{\triangle n}{n}$) measured at 250 GHz in vertically printed samples using a 0.4 mm nozzle and standard printing parameters with variation of print layer height. From Clark AT, Federici JF and Gatley I (2021) Effect of 3D printing parameters on the refractive index, attenuation coefficient, and birefringence of plastics in terahertz range. *Advances in Materials Science and Engineering* **2021**: 8276378.
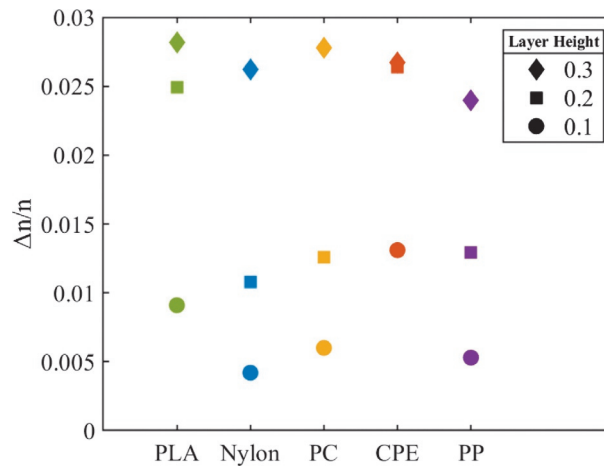
The samples were cut and their cross sections were viewed using a light optical microscope but no air gaps within the prints were discovered. It is plausible that the surface texture differences between the horizontal and vertical samples might cause these correlations. In a vertically printed sample, the THz beam is interacting with a repeating structure surface layer with features of similar size to its wavelength. Previously reported, increasing the surface roughness of various samples measured in the THz range has increased the uncertainty of thickness measurements as well as increased the measured values of real refractive indices (Burger et al., 2021; Fukuchi et al., 2013). Changes in the refractive index and attenuation coefficient based on a change in nozzle size and layer height were also measured and are shown in Clark et al. (2021).

Using the same samples, the birefringence dependent on varying printing parameters was also measured. Vertically printed samples show birefringence levels above the experimental uncertainty and are shown in Fig. 5. As the layer height of the samples increases, the birefringence present in the sample also increases. This trend is seen in every filament material. Additional stresses may be induced into the material as it is rapidly heated and cooled from printing temperature back to room temperature during the FDM 3D printing process. These large thermal fluctuations combined with forced extrusion could create a birefringence within the final structure as the layers are deposited on top of one another. Increasing in nozzle size from 0.4 mm to 0.8 mm causes an average of 125% decrease in birefringence, shown in (Clark et al., 2021). One possible explanation for this decrease is that with the larger nozzle size each layer of the sample is printed faster and, since each layer is printed faster, there is less elapsed time for that layer to cool. With shorter time between layers, there will be a decrease in the introduction of residual stresses into the material due to thermal differences between those layers. As shown in the slower printing 0.4 mm nozzle samples, thermal differences between layers will create a larger measurable birefringence than the faster printing 0.8 mm nozzle layers (Clark et al., 2021). These measurements showcase another application of THz NDE; the ability to measure and track changes to important optical characteristics of AM structures.

Refractive effects

THz radiation will undergo refraction when entering a sample at any angle other than normal incidence. This refraction leads to a redirection of the beam that needs to be accounted for in image reconstruction. This shortcoming can be mitigated in some cases using an index matching material. This material, typically a fluid, can be used to surround the sample, and be shaped in such a way as to create boundaries of normal incidence that couple the THz radiation into the sample by minimizing refraction and reflection of the beam as it interacts with the sample.

A simple example is provided by the study of insects embedded in ancient amber. Samples of Dominican amber (in which ancient termites are sometimes encased) typically have an irregular rounded shape. In order to remove most of the topological refractive effects, the round sample of amber is suspended in a cubical container filled with a liquid of similar refractive index to the amber, such as mineral oil. Under a perfect refractive index match, the surface topology of the sample will vanish because there will be no reflections from the surface of the sample, allowing inclusions within the sample to be studied free from distortions. Fig. 6 shows a measurement using a closely matched refractive index fluid to minimize the refractive effects caused by the amber matrix. Alternative methods of refractive correction algorithms are discussed in the next section.

THz computed tomography of additively manufactured components

The approach of 3D image reconstruction using computed tomography (CT) is illustrated using the parallel ray configuration of Fig. 7 to image a slice of an object. The line scans, which are a collection of measurements along parallel ray paths, are called projection measurements. The measured quantity can be transmission, absorption, time-of-flight, refractive index, or some other electromagnetic quantity. A projection measurement is a set of line integrals that represent the interaction between the incident radiation and the medium represented by a 2D function $f(x,y)$ that it interacts with and transmits through along one axis of measurement. Projection measurements are performed at multiple rotation angles θ. These projection measurements are the primary source of data for the tomographic reconstruction of the 2D slice through the object. Full 3D reconstruction is achieved by translating the object perpendicular to the page and acquiring data for each 2D slice.
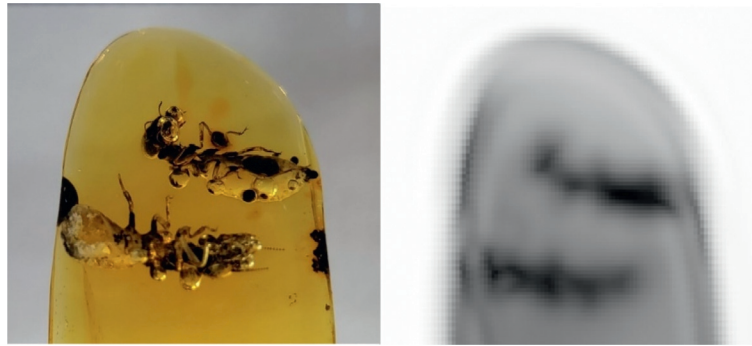

Fig. 6 (Left) Dominican amber sample. (Right) 0.5–2 THz frequency range integration image of the amber sample submerged in Fisher Scientific pure mineral oil, a closely matched refractive index fluid, to reduce refractive effects (Clark, 2022).
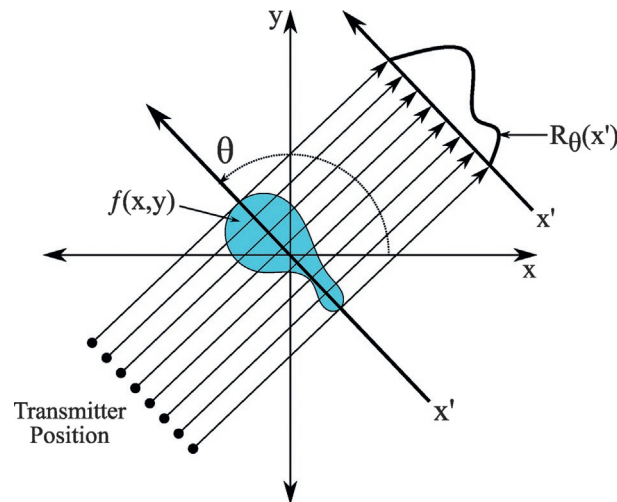

Fig. 7 Illustration of a parallel beam projection measurement where $f(x,y)$ is the two-dimensional (2D) function representing the sample and $R_\theta(x')$ is the resulting projection measured at angle θ (Clark, 2022).

A Radon transformation is a linear operator used to take a known function f in a 2D coordinate plane and represent it in what is known as the projection domain. A projection of an object can be represented by the sum of several sine waves. At each measured z value (see Fig. 7), a set of projections from discrete angles is then formed into a 2D representation of the object in the projection domain known as a sinogram (Taubmann et al., 2018). A sinogram is a stack of projection measurements that can be used to construct a tomographic image of the structure that was scanned.

Converting the sinogram measurements to a reconstructed tomographic image is an inverse problem. The sinogram measurements are used in various reconstruction methods such as the standard filtered back-projection (FBP) algorithm, iterative techniques such as the algebraic reconstruction technique (ART), or an even faster simultaneous algebraic reconstruction technique (SART) to create 2D tomographic images (Dhawan, 2003; Recur et al., 2011). Iterative reconstruction methods generally result in more accurate reconstructions but require much more computational power and time. The tomographic images, or "slices", are top-down views of the selected plane through the object scanned. By stacking these individual tomographic images and utilizing reconstruction software, it is possible to create a 3D reconstruction of the structure based on the chosen optical property or waveform attribute that was measured.

Despite the commonality of approach between X-Ray and THz CT, there are some major distinctions in applying computed tomography in the two different spectral regions. X-ray CT is much simpler than THz CT because X-Ray radiation travels through the target material in almost straight lines without much refraction, but THz waves are susceptible to refraction and loss of signal from boundaries: specifically, due to refraction at boundaries, reconstructed THz–CT images exhibit enhanced attenuation at the boundaries and also a distortion of the boundary shapes. Examples of the boundary effect can be seen in many papers on THz CT imaging (Ferguson et al., 2002; Mittleman et al., 1997; Zhang, 2003; Wang and Zhang, 2004; Chan et al., 2007). When elementary back-projection of filtered-projections (BFP) image reconstruction is utilized, only in the case of a low refractive index contrast material (Li et al., 2012; Kim et al., 2012; Lee et al., 2012; Nishina et al., 2012) can the refractive and reflective effects be ignored in the image reconstruction. Refraction of THz radiation by materials—unless the material is immersed in an index matching material—is therefore an inevitable aspect of THz CT.

Perraud et al. (2016) used THz CT to inspect 3D printed components for biomedical implants (PEEK) as well as for aviation components (polyamide). Their CT reconstruction algorithm accounts for a THz Gaussian beam profile. They observe that the finite beam size effect convoluted with the geometric effects (that is, the deflection of the THz beam by the refraction) distorts the reconstructed images and leads to a "systematic over-evaluation of the measured external dimensions and underestimation of the internal ones.". . ."After interaction with the object, [the] refraction effect of the THz beam makes it difficult to properly identify the amplitude since an important part of the signal is lost out of the detector. Moreover, each interface and nonparallel surfaces accentuate refraction losses and explain the discrepancies obtained for internal diameter measurements."

A small number of papers have studied the refraction/ boundary artifacts phenomenon and have tried to remove the prominent boundary effect phenomena by different methodologies. Abraham et al. (2010) introduce a multi-peak averaging method to eliminate boundary effects due to refraction losses of the THz beam inside the material. In applying this technique to 3D THz-CT images of a Teflon (refractive index 1.37) cylinder with a hole on it, the effect of the boundaries is reduced, but the boundaries are still visibility enhanced in the reconstructed image.

Using a completely different methodology, (Mukherjee et al., 2013) showed that by correcting for the two most dominant phenomena (i.e. steering of the THz beam and Fresnel reflection) prior to image reconstruction using filtered backpropagation, the boundary effect can be essentially eliminated. If the shape and refractive index of a 'standardized' object were known a-priori, then in principle the effects of Fresnel reflection and refraction would be removed from CT projection data prior to applying filtered backpropagation to reconstruct the image. Because the desired shape and materials of 3D printed structures are known a priori, it is possible to correct for the refraction effects of terahertz beam propagation.

More advanced image reconstruction methodologies are better suited to address the refraction effects of terahertz beam propagation. As an example, consider a more complicated structure such as the "C" shaped structure in Fig. 8 in which direction of a THz ray changes several times as it propagates through the structure. The BFP image reconstruction approach is not valid since the individual rays are not straight lines. The refraction from additional material boundaries in the ray's path might result from complicated surface geometries, printing infills less than 100% (i.e., not a solid object), or from the use of different materials and consequently different refractive indices in the printed structure. Clearly, for more complicated structure, another method such as Algebraic Reconstruction Techniques (ART), Landweber iteration, or SART (Dhawan et al., 2008; Dhawan, 2003; Tepe et al., 2017; Posodeder et al., 2022) rather than filtered backpropagation is required to reconstruct THz CT images.

As illustrated in Fig. 8, an ART reconstructive grid is defined with each pixel corresponding to a spatial location of the object to be imaged. Optical properties (e.g., absorption or refractive index) of the material are associated with each pixel location. If one propagates an X-ray through the structure (i.e., no refraction for Ray A), the ray sum p_i in the projection data can be expressed as

$$p_i = \sum_{j=1}^{N} w_{i,j} f_j \tag{6}$$

where $i = 1, \ldots, M$ and M is the number of projection rays. The weighting function $w_{i,j}$ represents the contribution from each pixel to the ray sum. The representation of Eq. (6) yields M equations for the N unknown pixel values. Conceptually, the pixel values are determined by comparing the measured projection ray values to those calculated from Eq. (6) and minimizing the error. For each iteration to minimize the error, the difference between the computed ray and measured projection ray sums is calculated and then distributed among the pixels in a weighted manner prior to the next iteration.
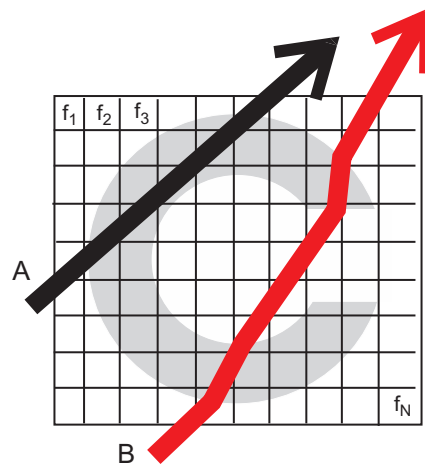
Fig. 8 Reconstruction grid with two rays which would define path sums for ART for rays passing through the "C" shaped structure. Ray A (black) illustrates ray propagation through the structure with no refraction present (e.g., X-Ray) and while Ray B (red) illustrates propagation with refraction present (e.g., THz).

In the generalized implementation of ART, the iterative process is initiated by pre-assigning values for each pixel. However, one can take advantage of the fact that for 3D printed components, the design values for the geometry and material properties of the 3D printed components are known a priori. Hence, the initial values for each pixel can be determined from the 3D design files for the component. Furthermore, one can integrate geometric ray tracing of the rays through the reconstruction grid to account for changes in the direction of an individual ray due to refraction as it propagates through the structure. Essentially, one needs to iteratively update both the ray paths and the optical properties of the pixels to reconstruct the THz CT image. Note that with this ART approach, multiple changes in the direction of a propagating ray due to refraction can easily be included as well as Fresnel reflection losses from boundaries. There is no longer the requirement, as is routinely assumed in conventional THz CT, that the THz rays propagate as straight lines through the test object.

Fig. 9 compares using three different reconstruction methods including back-projection of filtered-projections (BFP), simultaneous algebraic reconstruction technique (SART) reconstruction, and an ordered subsets expectation maximization (OSEM) method. These different reconstruction methods were used to create reconstructions of a white foam parallelepiped with two
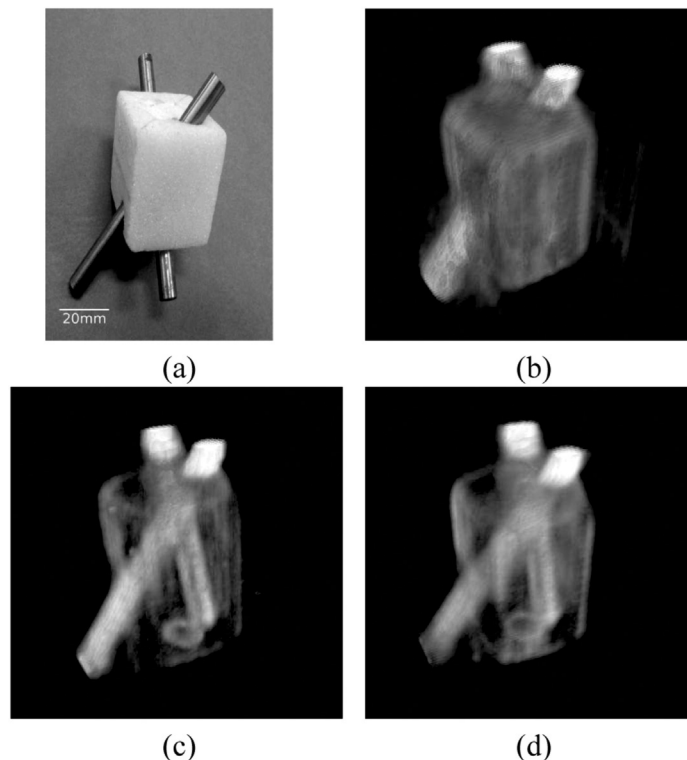

Fig. 9 Successful 3D CT reconstruction using THz NDE (240 GHz frequency) showcasing the differences between three different reconstruction methods. The object is a 30 mm cube size white foam parallelepiped with two oblique metallic bars (6 mm diameter). (a) Photograph of the 3D sample (b) BFP reconstruction (c) SART reconstruction (d) OSEM reconstruction. Reprinted with permission from Recur B, Younus A, Salort S, Mounaix P, Chassagne B, Desbarats P, Caumes JP and Abraham E (2011) Investigation on reconstruction methods applied to 3D terahertz computed tomography. *Optics Express* **19**: 5105–5117. © The Optical Society.
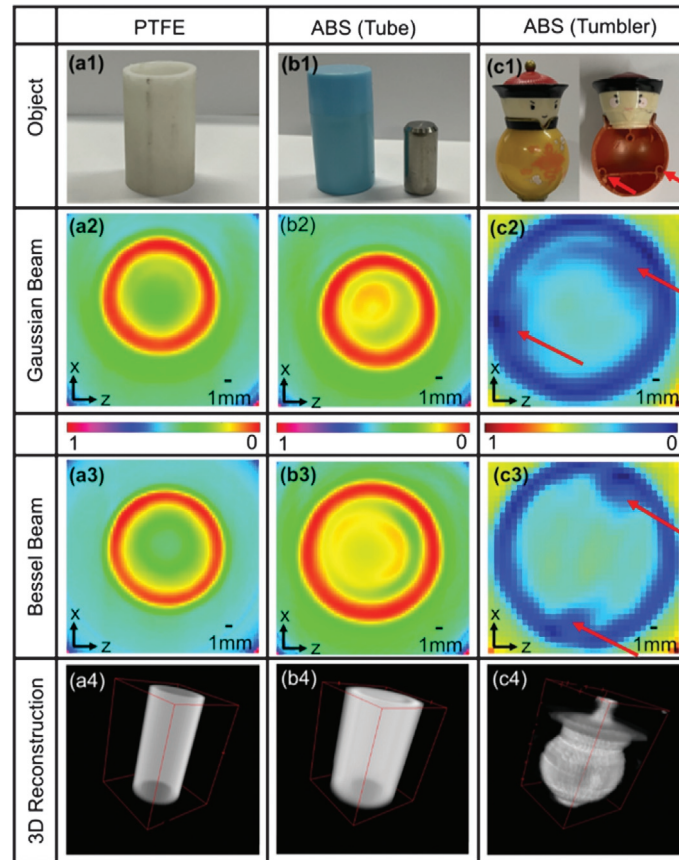
Fig. 10 3D CT reconstructions using THz NDE showcasing the use of Gaussian and Bessel beams for tomogram creation. Reprinted with permission from Wang D, Ning R, Li G, Zhao J, Wang Y and Rong L (2022) 3d image reconstruction of terahertz computed tomography at sparse angles by total variation minimization. *Applied Optics* **61**: B1–B7. © The Optical Society.

metal bars throughout. Different types of reconstruction methods are created to reduce or eliminate artifacts in the reconstructions. For example, BFP suffers largely from terahertz beam refraction that needs to be accounted for using corrective algorithms. This experiment was performed to show the ability in visualizing the internal structure of the foam nondestructively, while also showcasing the first application of SART and OSEM to THz CT (Recur et al., 2011). Fig. 10 shows THz CT being used on two different polymer tubes and a polymer tumbler. This figure is comparing the difference between using a Gaussian and Bessel beam for BFP reconstruction. It is shown that in these tomograms the Bessel beam reduces the effects of refraction at the boundaries allowing for a closer reconstruction to the original sample (Wang et al., 2022).

The accuracy to which complex shapes can be resolved using ART techniques is shown in Fig. 11 (Posodeder et al., 2022). Using the design geometry as an a priori guess as to the shape and refractive index properties of the 3D printed structure, geometric optics (i.e., Snell's law) is used to propagate the terahertz radiation through the 'guess' reconstructed structure in order to mathematically correct for refractive effects. Based on a minimization of the error in comparing the measured and reconstructed image, the initial guess as to the shape and refractive index properties of the object are updated for the next iteration in the optimization algorithm. The L1 regularization algorithm, which assumes that large parts of the sample consist of air, produces a reconstructed image whose wall thicknesses most closely match the physical sample.

Another limitation in THz CT compared to X-ray CT is its spatial resolution. Since the wavelength of terahertz radiation (300 μm at 1 THz) is much larger than the wavelength of X-rays, the spatial resolution of X-rays can be significantly better due to diffractive effects. As an example, Ref. (Markl et al., 2017) compared the performance of X-ray and THz CT on pharmaceutical solid dosage forms. Two dosage forms were fabricated by FDM; a single compartment structure with a nominal shell thickness of 0.7 mm and a two-compartment structure with each shell 1.4 mm thick. A key challenge in additively manufactured pharmaceutical dosage forms is the quality control of each single dosage unit. Their results show that X-ray CT provides very detailed information about the microstructure and defects in the 3D print. However, due to the long acquisition and reconstruction times of X-ray CT images, it is not feasible to perform quality control on every printed dosage form. While terahertz imaging, due to its rapid acquisition of depth profiles, could enable quality control of a much larger number of samples, there is insufficient spatial resolution in the terahertz images to extract the essential information about the microstructure.
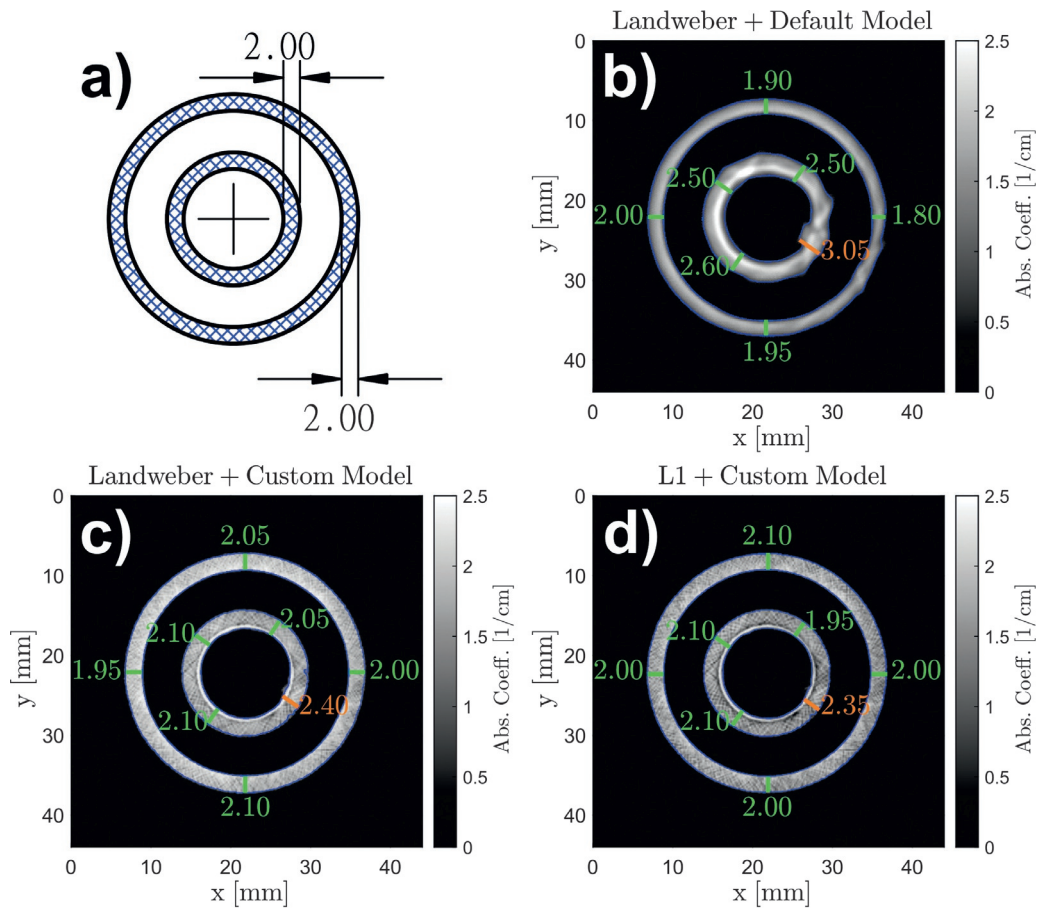
Fig. 11   Results of a 2D THz CT reconstruction of a 3D printed polypropylene double tube sample. (A) The nominal design structure including the thicknesses of the tube wall. Three different image reconstructions of the sample using (B) Landweber iteration plus a default model as implemented in (Fosodeder et al., 2021). No refractive corrections are included (c) Landweber iteration with refraction corrections and (d) L1 regularization with refractive corrections. The last reconstruction gives the most accurate wall thicknesses. Reprinted with permission from Posodeder P, Frank SV and Rankl C (2022) Highly accurate THz-CT including refraction effects. *Optics Express* **30**: 3684–3699. © The Optical Society.

Despite the limited spatial resolution of THz CT compared to X-ray CT, there are complementary approaches one might use to offset the limited spatial resolution of terahertz imaging. For the present example, in which the microstructure and porosity are critical to the functionality of the dosage form, one might be able to employ an index matching fluid to fill in open pores. Introduction of the index matching fluid would reduce the scattering from the porous material enabling a quantitative evaluation of the microstructure and porosity (Naftaly et al., 2020).

Birefringence

It is well-known that stress-induced birefringence occurs in many transparent materials when load is applied (Hecht, 2017). Consequently, the stress-induced birefringence enables photoelasticity measurements to experimentally visualize stress analysis in transparent material (Dally, 1978). In a stress-less experiment with an isotropic (non-birefringent) material placed between two polarizers whose transmission axes are orthogonal, the light which passes through the first polarizing filter maintains its polarization as it propagates through the isotropic material; therefore no light emerges from the second crossed polarizer. However, if the material experiences either applied stress or intrinsic stress, the induced birefringence rotates the plane of polarization of light propagating through the material resulting in some transmission through the second crossed polarizing filter.

The advantage of using terahertz radiation rather than visible radiation for birefringence measurements is that terahertz radiation can be used to probe non-metallic materials which are opaque to visible light. Example materials include plastics, ceramics, as well as composite materials. Several experimental configurations of terahertz birefringence instrumentation have been demonstrated including a very simple measurement in which the arrival times of terahertz pulses with various polarization orientations are measured (Clark et al., 2021). From the difference in pulse arrival times for various polarization orientations, the magnitude and direction of sample birefringence may be calculated.

A cross-polarizer experimental geometry as introduced by Kang et al. (2021) enabled precise birefringence measurements in the terahertz frequency range. Fig. 12 illustrates the relative orientations of the polarizers as well as the relative orientation of the fast
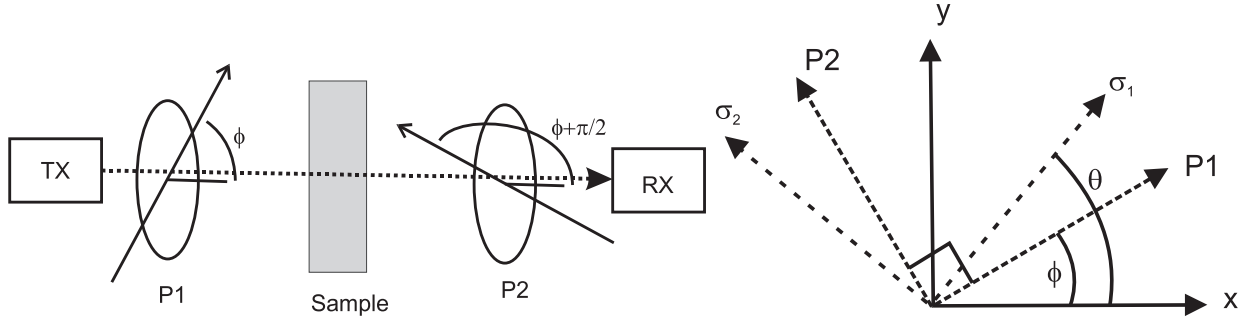
Fig. 12 Experimental configuration for measurement of birefringence in a transmission mode. (a) relative positions of the transmitter/polarizer P1 module, birefringent sample, and receiver/polarizer P2 module. (b) orientation of transmission axes of polarizers P1 and P2, relative to the laboratory horizontal x-axis. The terahertz pulse is propagating into the page. The fast σ_1 and slow σ_2 axes of the birefringent material are assumed to be orthogonal.

and slow refractive index axes of the sample. Rather than analyzing the polarization properties of the transmitted terahertz waves in Fig. 12 using a Jones Matrix approach (as was performed in Kang et al., 2021), here an alternative method is used which is more amenable to the time-domain.

For simplicity, it is assumed that the sample can be treated as a uniaxial birefringent material in which the principle stress axes are perpendicular to the propagation direction of the terahertz waves. The electric field after transmission through polarizer P1 in Fig. 12 can be expressed as

$$E_{TX} = E_{inc}(t)(\widehat{x}\cos\phi + \widehat{y}\sin\phi) \tag{7}$$

where ϕ is the angle between the horizontal x-axis and the transmission axis of polarizer P1. As the terahertz pulse enters the sample, the vector components of the electric field are written in terms of the basis vectors of the fast (lower refractive index) and slow (higher refractive index) of the material with the fast axis oriented at an angle θ with respect to the horizontal x-axis:

$$\widehat{x} = \widehat{\sigma}_1 \cos\theta - \widehat{\sigma}_2 \sin\theta \tag{8}$$

$$\widehat{y} = \widehat{\sigma}_1 \sin\theta + \widehat{\sigma}_2 \cos\theta \tag{9}$$

The electric field just as it enters the sample, using Eqs. (7–9), can be expressed as

$$E_{s\_in}(t) = E_{inc}(t)\tau_{as}[\widehat{\sigma}_1(\cos\phi\cos\theta + \sin\phi\sin\theta) + \widehat{\sigma}_2(\sin\phi\cos\theta - \cos\phi\sin\theta)] \tag{10}$$

where τ_{as} is the transmission coefficient in propagating from air into the material. Since the electric field is expressed in terms of the basis for the fast and slow axes, the additional time delay for propagation through the sample and back into the air can be expressed as

$$E_{s\_out}(t) = \tau_{as}\tau_{sa}[\widehat{\sigma}_1 E_{inc}(t + \Delta t_{\sigma_1})(\cos\phi\cos\theta + \sin\phi\sin\theta) + \widehat{\sigma}_2 E_{inc}(t + \Delta t_{\sigma_2})(\sin\phi\cos\theta - \cos\phi\sin\theta)] \tag{11}$$

where the propagation times for the two principal axes in the material are given by $\Delta t_{\sigma_1} = n_{\sigma_1}L/c_o$ and $\Delta t_{\sigma_2} = n_{\sigma_2}L/c_o$. The product $\tau_{as}\tau_{sa}$ accounts for any losses in transmission due to reflection of a portion of the terahertz pulse at the air-sample interfaces.

After propagating the terahertz pulse through the sample, one translates Eq. (11) back into the laboratory x-y frame using

$$\widehat{\sigma}_1 = \widehat{x}\cos\theta + \widehat{y}\sin\theta \tag{12}$$

$$\widehat{\sigma}_2 = -\widehat{x}\sin\theta + \widehat{y}\cos\theta. \tag{13}$$

Finally, the resulting electric field through the polarizer P2 is calculated by taking the dot product with the transmission axis polarization of P2 given by $\widehat{P2} = -\widehat{x}\sin\phi + \widehat{y}\cos\phi$. After rearranging terms, the final electric field detected by the receiver can be expressed as

$$E_{RX}(t) = \tau_{as}\tau_{sa}[E_{inc}(t + \Delta t_{\sigma_1}) - E_{inc}(t + \Delta t_{\sigma_2})](\sin\theta\cos\theta(\cos^2\phi - \sin^2\phi) + \sin\phi\cos\phi(\sin^2\theta - \cos^2\theta)) \tag{14}$$

As a quick check, when there is no birefringence, then $\Delta t_{\sigma_1} = \Delta t_{\sigma_2}$ and the detected electric field vanishes. Likewise, if $\theta = \phi$ then the polarizers P1 and P2 are along the principal stress and birefringence axes yielding no detectable electric field since for this orientation of the sample relative to the polarizers, the birefringence does not rotate the polarization of the incident terahertz pulse.

The next step is to evaluate the difference in the two time-shifted electric fields $E_{inc}(t + \Delta t_{\sigma_1}) - E_{inc}(t + \Delta t_{\sigma_2})$. To facilitate the calculation, Fourier transforms as defined below will be utilized

$$f(\nu) = \int_{-\infty}^{\infty} f(t)e^{-i2\pi\nu t}dt \tag{15}$$

$$f(t) = \int_{-\infty}^{\infty} f(v) e^{i2\pi vt} dv. \tag{16}$$

If one assumes that the refractive indices along the principle stress directions are constant as a function of frequency, the Fourier transform of the time-shifted incident electric field may be evaluated as

$$E_{\sigma_1}(v) = \int_{-\infty}^{\infty} E_{inc}(t + \Delta t_{\sigma_1}) e^{-i2\pi vt} dt = E_{inc}(v) e^{i2\pi v \Delta t_{\sigma_1}}. \tag{17}$$

This result is expected because, in the frequency domain, the time delay is manifested as a simple multiplication by a phase factor. Using Eq. (17), the difference in the time-shifted electric fields of Eq. (14) can be evaluated as

$$E_{inc}(t + \Delta t_{\sigma_1}) - E_{inc}(t + \Delta t_{\sigma_2}) = \int_{-\infty}^{\infty} (E_{\sigma_1}(v) - E_{\sigma_2}(v)) e^{i2\pi vt} dv. \tag{18}$$

Factoring out the average phase shift on the right-hand side of the equation gives

$$E_{inc}(t + \Delta t_{\sigma_1}) - E_{inc}(t + \Delta t_{\sigma_2}) = \int_{-\infty}^{\infty} E_{inc}(v) e^{i2\pi v\left(\Delta t_{\sigma_2} + \Delta t_{\sigma_1}\right)/2} \left(e^{i2\pi v\left(\Delta t_{\sigma_1} - \Delta t_{\sigma_2}\right)/2} - e^{-i2\pi v\left(\Delta t_{\sigma_1} - \Delta t_{\sigma_2}\right)/2} \right) e^{i2\pi vt} dv \tag{19}$$

$$= -\int_{-\infty}^{\infty} 2iE_{inc}(v) e^{i2\pi v\left(\Delta t_{\sigma_2} + \Delta t_{\sigma_1}\right)/2} \sin(\pi v \Delta n L/c_o) e^{i2\pi vt} dv. \tag{20}$$

where the birefringence $\Delta n = (n_{\sigma_2} - n_{\sigma_1})L/c_o$. In the limit that the birefringence is small such that $\pi v \Delta n L/c_o \ll 1$, the sine function can be approximated such that

$$E_{inc}(t + \Delta t_{\sigma_1}) - E_{inc}(t + \Delta t_{\sigma_2}) \simeq -2\pi i \frac{L\Delta n}{c_o} \int_{-\infty}^{\infty} v E_{inc}(v) e^{i2\pi v\left(\Delta t_{\sigma_2} + \Delta t_{\sigma_1}\right)/2} e^{i2\pi vt} dv \tag{21}$$

$$\simeq -\frac{\Delta n L}{c_o} \frac{d}{dt}\left[E_{inc}\left(t + \frac{\Delta t_{\sigma_2} + \Delta t_{\sigma_1}}{2}\right)\right] = \frac{\Delta n L}{c_o} \lim_{\Delta t_0 \to 0} \left[\frac{E_{inc}\left(t + \frac{\Delta t_{\sigma_2} + \Delta t_{\sigma_1}}{2}\right) - E_{inc}\left(t + \Delta t_0 + \frac{\Delta t_{\sigma_2} + \Delta t_{\sigma_1}}{2}\right)}{\Delta t_0}\right] \tag{22}$$

where on the right-hand side of Eq. (22) the time derivative of the incident electric field pulse is approximated as a finite difference. This equation justifies the following model for the difference in the time-delayed incident pulses

$$E_{inc}(t + \Delta t_{\sigma_1}) - E_{inc}(t + \Delta t_{\sigma_2}) \simeq \Delta n A E_{diff}(t) \tag{23}$$

where Δn is the material birefringence, $E_{diff}(t) = E_{inc}(t + (\Delta t_{\sigma_2} + \Delta t_{\sigma_1})/2) - E_{inc}(t + \Delta t_0 + (\Delta t_{\sigma_2} + \Delta t_{\sigma_1})/2)$, and $A = L/c_o\Delta t_o$ is a scaling factor. The differential electric field pulse E_{diff} can be generated mathematically by subtracting the incident electric field waveform shifted in time by Δt_o, from the incident waveform. For simplicity, a value of $\Delta t_o = 0.1$ ps is used which is the time interval in the terahertz waveforms digitized by the T-Ray 5000 system.

Combining Eqs. (14) and (23) gives the detected terahertz time-domain waveform as

$$E_{RX}(t) = \tau_{as}\tau_{sa}\left[\Delta n A E_{diff}(t)\right]\left(\sin\theta\cos\theta\left(\cos^2\phi - \sin^2\phi\right) + \sin\phi\cos\phi\left(\sin^2\theta - \cos^2\theta\right)\right). \tag{24}$$

The goal of the terahertz birefringence measurement is to measure the detected terahertz waveform at two different values of ϕ to determine uniquely the birefringence magnitude Δn and the stress principle stress direction θ of the material. Evaluating the measured time-domain waveform for the polarizer P1 making angles of $\phi = 0°$ and $\phi = 45°$ with respect to the x-axis (polarizer P2 is orthogonal to P1 for both values of ϕ) gives two equations for the measured waveforms

$$E_0(t) = \tau_{as}\tau_{sa}\left[\Delta n A E_{diff}(t)\right](\sin\theta\cos\theta), \tag{25}$$

$$E_{45}(t) = \tau_{as}\tau_{sa}\left[\Delta n A E_{diff}(t)\right]\left(\sin^2\theta - \cos^2\theta\right)/2. \tag{26}$$

By extracting the pulse amplitudes of the waveforms denoted by E_0 and E_{45}, the stress direction

$$\frac{E_o}{E_{45}} = \frac{2\sin\theta\cos\theta}{\sin^2\theta - \cos^2\theta} = -\tan 2\theta \tag{27}$$

may be calculated by dividing Eqs. (25) and (26). This is the same result as derived by Kang et al. (2021).

The magnitude of the birefringence can be determined by measuring the amplitudes of the waveforms denoted by E_0, E_{45}, and $\tau_{as}\tau_{sa}E_{diff}$. Eqs. (25) and (26) may be squared and added to yield

$$\Delta n = \frac{2c_o\Delta t_o}{L}\sqrt{\left(\frac{E_o}{\tau_{as}\tau_{sa}E_{diff}}\right)^2 + \left(\frac{E_{45}}{\tau_{as}\tau_{sa}E_{diff}}\right)^2}. \tag{28}$$

Note that the denominator of Eq. (28) takes into account the reflective losses of the incident electric field pulse as it propagates through the air-sample interfaces. An added benefit in measuring the time shifts Δt_{σ_1} and Δt_{σ_2} referenced to no sample in the

terahertz beam path enables one to normalize out the thickness from Eq. (28). In this case the average of the time shifts may be written as

$$\frac{\Delta t_{\sigma_1} + \Delta t_{\sigma_2}}{2} = \frac{L}{c_o}\left(\left(\frac{n_{\sigma_1} + n_{\sigma_2}}{2}\right) - 1\right) = \frac{L}{c_o}\left(n_{average} - 1\right). \tag{29}$$

Dividing Eq. (28) by Eq. (29) gives the relative birefringence as

$$\frac{\Delta n}{n_{average} - 1} = 2\frac{\Delta t_o}{(\Delta t_{\sigma_1} + \Delta t_{\sigma_2})/2}\sqrt{\left(\frac{E_o}{\tau_{as}\tau_{sa}E_{diff}}\right)^2 + \left(\frac{E_{45}}{\tau_{as}\tau_{sa}E_{diff}}\right)^2}. \tag{30}$$

Evaluation of Eq. (30) requires measurement of the amplitudes and arrival times of the three waveforms denoted by E_o, E_{45}, and $\tau_{as}\tau_{sa}E_{diff}$.

Extraction of the stress direction from Eq. (27) and the relative birefringence from Eq. (30) requires measurement of 4 THz pulse waveforms. The time-domain waveforms through the sample with polarizers P1 and P2 oriented orthogonally as illustrated in Fig. 12 with $\phi = 0°$ and $\phi = 45°$ correspond to E_o and E_{45}. The measured waveform through the sample with P1 and P2 oriented parallel to each other corresponds to $\tau_{as}\tau_{sa}E_{inc}(t + (\Delta t_{\sigma_2} + \Delta t_{\sigma_1})/2)$. The waveform $\tau_{as}\tau_{sa}E_{diff}$ is calculated by shifting the waveform by one time slot (corresponding to 0.1 ps for the Terametrix T-Ray 5000 system) and subtracting the shifted waveform from the unshifted waveform. The last required waveform is one with the sample removed which essentially measures $E_{inc}(t)$. The time delay of the waveform with the sample present compared to the sample removed effectively measures $(\Delta t_{\sigma_2} + \Delta t_{\sigma_1})/2$.

The amplitudes of the measured waveforms are calculated using a deconvolution calculation. The amplitudes and arrival times for the E_o and E_{45} waveforms are mathematically determined by a deconvolution process using Matlab software with $\tau_{as}\tau_{sa}E_{diff}$ as the reference pulse for the deconvolution. The deconvolution is performed using Fourier transforms

$$E_{deconv}(t) = A_o\,ifft\left(fft(E(t))/fft\left(E_{ref}(t)\right)\left(\exp\left(-(2\pi v t_w)^2/2\right)\right)\right) \tag{31}$$

where $E_{ref}(t)$ denotes a reference waveform. The parameter $t_w = 4$ ps represents a smoothing time window. The normalization constant A_o is chosen such that the amplitude of a deconvoluted waveform with itself (i.e., $E(t) = E_{ref}(t)$) is unity. Once the deconvoluted waveform is calculated, the amplitude A and arrival time t_a of the deconvoluted pulse is determined by fitting the peak of the waveform to a Gaussian shape $G(A, t_a, c) = A\exp\left(-((t - t_a)/c)^2\right)$. Typically, the best fit is performed on data only within ± 0.7 ps of the deconvoluted waveform peak. The arrival time $(\Delta t_{\sigma_2} + \Delta t_{\sigma_1})/2$ is calculated by deconvolving the waveform $\tau_{as}\tau_{sa}E_{inc}$ with $E_{inc}(t)$ as the reference.

As an example, a 10 mm sheet of extruded high-density polyethylene (HDPE) is characterized. Fig. 13 shows experimental measurements of the birefringence from a small piece of extruded HDPE. Fig. 13a shows the measured received electric field amplitude as a function of angle of rotation φ for the orthogonal polarizers. Note that the theoretical fit to the experimental data is very good. The images of Fig. 13b and c show 2D mages of the local direction of the intrinsic stress in the sample as well as the measured normalized birefringence given by $\Delta n/(n_{avg} - 1)$ where Δn is the difference in refractive index along the two principle stress directions, and n_{avg} is the average refractive index of the material.
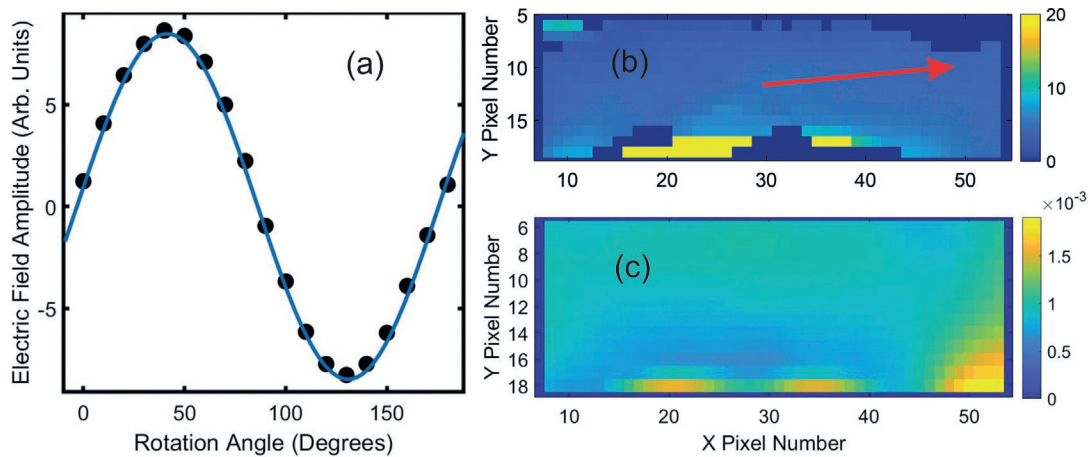

Fig. 13   (a) at a fixed point in the sample, measurement of the amplitude of the received electric field amplitude as a function of angle of rotation φ for the orthogonal polarizers. The theoretical line is from Eq. (14). (b) extracted stress angle in units of degrees from Eq. (27) and (c) normalized birefringence from Eq. (30).

Multilayer paint stacks

Terahertz NDE of multilayer paints

The analysis geometry is illustrated in Fig. 14a for an $N = 3$ layer paint stack. The terahertz pulse is incidence from air onto N dielectric layers before encountering a metallic substrate. Each layer is characterized by a thickness d_j and complex refractive index $\tilde{n}_j$. There are three basic approaches to analyzing the THz reflectivity data. The first approach is to deconvolve the reflected terahertz waveform with a reference waveform which is acquired by reflection from a perfect metal. The peaks in the deconvolved waveform represent reflections from the various material boundaries in the multilayer stack. Application of this approach is discussed in more detail in Section "Results".

A second approach is to convert the time-domain THz waveform to the frequency domain through a Fourier transform. Analysis and extraction of the layer thicknesses and their refractive indices (both real part and imaginary part) are performed by fitting the measured reflectivity spectra to a theoretical model of multiple reflections through a multi-layer stack of layers. This method can be effective for relatively thick layers. However, as the layers become thinner, the reflected THz waveforms significantly overlap in time.

As described in van Mechelen et al. (2014), a stratified sample structure such as a paint layer stack, is difficult to analyze in the frequency domain since the reflectivity $R(\omega)$ has multiple internal reflections from the various layer boundaries. Moreover, in order to extract the refractive index by fitting the experimentally measured reflectivity to a model of the reflectivity, one would typically assume that the refractive index was real (i.e., no absorption due to the imaginary refractive index) and frequency independent. While modeling of the refractive index as primarily real and frequency independent reduces the number of fitting parameters to the experimental data, it was not a realistic description of the paint layers.

A superior method of analyzing stratified paint stack structures is to use realistic models for the frequency-dependent complex refractive index as well as fitting the theoretical model to the measured experimental data in the time-domain (van Mechelen et al., 2014; Krimi et al., 2016) rather than the frequency domain. The main benefit of the time-domain fitting is the stratified dispersive model which parameterizes each layer with a small number of fitting parameters enabling simultaneous extraction of the individual electromagnetic material parameters in multilayer structures. For application to multilayer paint structures, many dielectrics such as the polymers used in paint obey a Debye dielectric relaxation model. For this model, the frequency (ω) dependent index of refraction of the layer j material is given by

$$\tilde{n}_j(\omega) = \left(\varepsilon_j^\infty + \frac{\varepsilon_j^s - \varepsilon_j^\infty}{1 + i\omega\tau_j} \right)^{1/2} \tag{32}$$

where ε_j^∞ is the permittivity at the high-frequency limit, ε_j^s is the static, low-frequency permittivity, and τ_j is the characteristic relaxation time of the jth paint layer. The real part of the refractive index controls the time delay of the THz pulse or equivalently the speed of the THz pulse through the material. The imaginary part of the refractive index is responsible for the absorption of the THz pulse as it propagates through a layer.

As summarized by Krimi et al. (2017), the typical analysis process involves three steps: calibration, mathematical modeling of the terahertz propagation through the multilayer structure, and optimization. In the calibration step, a reference waveform is measured by replacing the paint stack layer with a flat metallic mirror. Since the front surface of the mirror cannot be placed in exactly the same plane as the front surface of the paint stack, the analysis incorporates an overall time delay ξ between the time-domain reference and reflected pulses. The calibration step may also include terahertz measurements of individual layers of each material to extract their complex refractive indices and Debye model fitting parameters.

The modeling step mathematically propagates an input terahertz pulse waveform through the multilayer stack to calculate the resulting reflected waveform. The mathematical modeling can be typically performed first by Fourier transforming the input
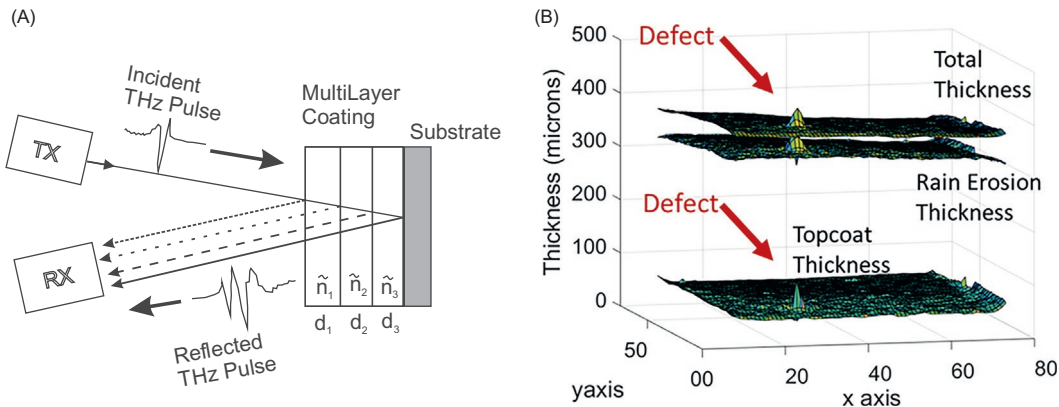

Fig. 14 (a) Illustration of terahertz reflection from multilayer paint coating. The transmitter and receiver are indicated by TX and RX, respectively. Each layer is parameterized by its thickness d_j and its complex refractive index $\tilde{n}_j$. After the incident pulse waveform interacts with the paint stack, the reflected THz waveform is measured. (b) A reconstructed 3D thickness image of a two-layer sample. The presence of a defect in the coating is indicated by the red arrows.

time-domain waveform into the frequency domain. The input waveform is then propagated through the multilayer stack by an optical transfer matrix method. As an example, a Debye dielectric relaxation model can be assumed for each non-metallic paint layer. The $j = 0$ layer is assumed to be air with $n_o = 1$. The parameter N represents the number of dielectric layers such that the metal substrate is the $N + 1$ layer. In the metal substrate, various models can be used to model the metal. One option is to use a Drude model for metal for which

$$\tilde{n}_{N+1}(\omega) = \left(\frac{\varepsilon_{N+1}^{\infty}}{\varepsilon_o} - i \frac{\sigma_o}{\varepsilon_o \omega} \frac{1}{(1 + i\omega\tau_{N+1})} \right)^{1/2} \tag{33}$$

where σ_o is the substrate's static conductivity, and ε_o denotes the vacuum electric permittivity. If the dielectric layers and metallic layer are characterized as part of the calibration step, then the Debye parameters ε_j^{∞}, ε_j^s, and τ_j as well as the metallic layer parameters, $\varepsilon_{N+1}^{\infty}$, σ_o, and τ_{N+1} are known for each layer. Alternatively, they could also be determined in the optimization step.

Given the functional form for the complex refractive indices and layer thicknesses, an incident pulse is propagated through the multilayer coating/substrate combination. One approach is to use an optical transfer matrix approach (Saleh and Teich, 1991). At each interface, it is assumed that the incident electromagnetic wave interacts at near normal incidence so that using Fresnel coefficients, the matrix representing the boundary is given by

$$P_{j,j+1}(\omega) = \frac{1}{2n_{j+1}} \begin{pmatrix} \tilde{n}_{j+1} + \tilde{n}_j & \tilde{n}_{j+1} - \tilde{n}_j \\ \tilde{n}_{j+1} - \tilde{n}_j & \tilde{n}_{j+1} + \tilde{n}_j \end{pmatrix}. \tag{34}$$

After propagating through an interface between adjacent layers, the transmitted light propagates through the thickness d_j of each layer. As the wave propagates through each layer, it experiences a frequency-dependent phase shift and is expressed through the diagonal matrix

$$D_j(\omega) = \begin{pmatrix} e^{-i\omega d_j \tilde{n}_j / c_o} & 0 \\ 0 & e^{i\omega d_j \tilde{n}_j / c_o} \end{pmatrix} \tag{35}$$

where d_j is the thickness of each optical layer, and c_o is the speed of light in a vacuum. In order to calculate the total effect, these matrices are cascaded layer by layer through the product

$$M(\omega) = \prod_{j=0}^{N} D_j P_{j,j+1} = \begin{pmatrix} M_{11} & M_{12} \\ M_{21} & M_{22} \end{pmatrix}. \tag{36}$$

The matrix Eq. (36) is known as the optical transfer matrix and completely characterizes the transmission and reflection in the multi-layered system. The reflectivity from the paint stack is calculated using the optical transfer matrix from

$$R(\omega) = \frac{M_{21}(\omega)}{M_{11}(\omega)}. \tag{37}$$

Lastly, there is an optimization step in which the thicknesses of the various layers are optimized in order to minimize the error between the measured time-domain reflected waveform and the waveform predicted by the mathematical modeling. The time-domain reflected electric field from an N-layer paint coating may be expressed as

$$E_R(t) = \mathcal{F}^{-1} \left[e^{-2\pi i \xi} R(\omega) \mathcal{F}[E_I(t)] \right] \tag{38}$$

where $\mathcal{F}[E_I(t)]$ is the Fourier transform of the incident Terahertz pulse. The analysis incorporates an overall time-delay ξ between the time-domain reference and reflected pulses. If the Debye model parameters for each layer have not been determined in the calibration step, they could be determined in the optimization step. Multiplying the Fourier Transform of the incident electric field by the reflectivity Eq. (37) and the overall phase shift effectively accounts for the propagation of the THz pulse through the various layers of the paint layer stack. The inverse Fourier transform converts the frequency-domain back into a time-domain pulse. The time-domain reflected pulse depends on the refractive indices and thicknesses of each paint layer, the reflectivity of the metallic substrate, and the overall time delay ξ.

Extraction of best-fit parameters is accomplished using a minimization algorithm to optimize the fitting parameters by minimizing the difference in the measured terahertz waveform compared to the waveform generated from Eq. (38) with the fitting parameters. As an example, a least-squares fitting process could be used as outlined below. To this end, let m be the number of fitting parameters. For example, with a two-layer model there are 2 paint layer thicknesses, there are 6 Debye parameters for the paint layers, 3 Drude parameters for the metal substrate, and an overall time delay for a total of $m = 12$ parameters. The measured data $E_{data}(t)$ is defined over some time window $[0, T]$. While the maximum value of $T = 160$ ps could be used since the Tray 5000 THz instrumentation used in this project records a 160 ps window of data, the time window is restricted to a 65 ps window centered on the main structure of the terahertz pulse (Fig. 15). The computational problem can be expressed as minimizing the squares of the error between the measured and fitted time-domain data. More precisely,
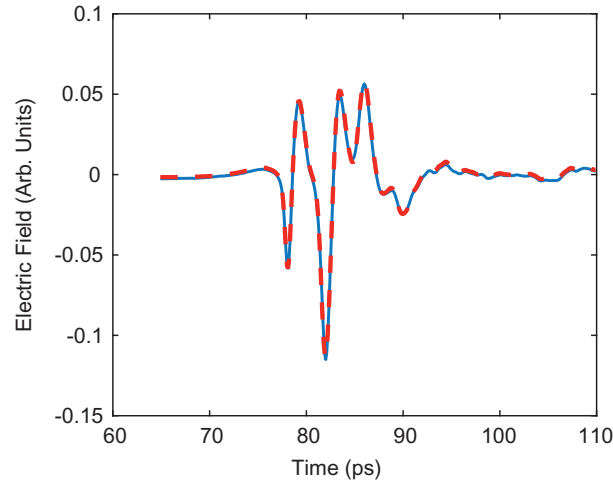
Fig. 15   Comparison of experimental reflected terahertz waveform (blue) to theoretical fit (red) using a two layer model.

$$\min_{\vec{P} \in \mathbb{R}^m} Error = \min_{\vec{P} \in \mathbb{R}^m} \left[\frac{1}{2} \left\| E_{data}(t) - E_R\left(\vec{P}, t\right) \right\|_{L^2([0,T])}^2 \right] \tag{39}$$

where $\vec{P}$ is a vector storing the m fitting parameters, and the fitting parameters must be part of a physically realizable parameter space (for example the thicknesses must be positive values). The norm defining the error is given by

$$\left\| \cdot \right\|_{L^2([0,T])} = \left(\int_0^T \left| \cdot \right|^2 dt \right)^{1/2}, \tag{40}$$

and $E_R\left(\vec{P}, t\right)$ is the parameter-dependent electric field computed in the frequency domain and mapped back to the time-domain through Eq. (38). The norm of the difference $E_{data}(t) - E_R\left(\vec{P}, t\right)$ measures the misfit, over the time-domain $[0, T]$, between the experimentally obtained data and the reflected electric field. The integration required by the norm is computed numerically via the trapezoidal rule.

As an example of the quality of the fit, Fig. 15 shows the experimentally measured and fitted electric field for a two-layer paint stack consisting of a UV topcoat, rain erosion layer, and metallic substrate (assumed to be a perfect metal). This data represents one pixel on a 2D painted sample. By recording the terahertz reflected waveforms on a pixel-by-pixel basis, refractive index and layer thickness maps similar to those in Fig. 14b may be extracted from the terahertz imaging data.

In adapting the terahertz pulsed imaging technique to real-time evaluation of paints, attention must be given to rapid processing of the images and reducing the computational time of the minimization algorithm. Krimi et al. (2017) have shown that utilizing Rouard's method (Krimi et al., 2016) rather than an optical transfer matrix approach enables one to reduce the computational time by a factor of 1.7 and the graphics processing unit (GPU) allocated memory by a factor of about 2.3. The methodology of (Krimi et al., 2017) utilizes a genetic algorithm optimization rather than a least squares optimization to provide best-fit parameters. This approach enables resolution of individual layer thicknesses of typically 7 μm with an absolute accuracy of less than 1 μm. Terahertz nondestructive monitoring of automobile multilayer paints has in fact been implemented on a limited scale in industrial automobile factories (https://das-nano.com/success-story/volkswagen/).

Terahertz NDE of paint corrosion

While terahertz pulse imaging has been adapted for industrial quality control measurements of paint layer thicknesses, another application of the methodology is detection of underlying corrosion of multilayer structures. To a large extent, the same terahertz instrumentation and methodology which was developed to assess the fabrication of multilayer structures can be used to assess the structure's degradation due to corrosion. An early example is the characterization of corrosion under Space Shuttle tiles which used the same instrumentation which was developed to inspect sprayed-on foam insulation (Anastasi et al., 2007).

Several studies demonstrating the feasibility of corrosion detection by terahertz imaging have been reported. As an example, one study (Tu et al., 2021) created buried corrosion layers by painting over rusted areas to create a 'hidden' corrosion defect. By comparing the terahertz pulse shape where no rust was present compared to a rusted area under the paint, it was readily observable that the terahertz pulse shape was significantly changed by the presence of rust. Changes in terahertz pulse shape were also present for which adjacent paint layers separated and also when the coating became detached from the substrate (some reports refer to the detachment of the coating from the substrate as 'blistering'). The change in pulse shape due to delamination of different

coating layers can be easily understood due to the presence of additional material boundaries which partially reflect the propagating terahertz radiation as well as additional time delays between pulse peaks as the spatial separation between layers increases (Dong et al., 2017).

Using a similar sample fabrication method, (Fuse et al., 2012) tested the viability of rust detection hidden under epoxy using carbon steel plates as substrates. Rusted areas on the substrate were created by placing a few drops of salt solution on its surface. After wiping off the residual solution, epoxy resin was used to cover the substrate surface. Terahertz reflection measurements showed that the rust strongly attenuates the terahertz radiation compared to uncorroded metal enabling sufficient contrast in terahertz pulsed imaging reflection measurements to detect the presence of the buried rust.

In a follow-up paper (Fuse et al., 2016), the technique was extended to higher terahertz frequencies using a quantum cascade laser (QCL) as the terahertz source and a terahertz camera for detection. Samples were exposed to a coastal environment for 27 months. The buried substrate surface corrosion resulted in an increase in surface roughness which increased the scattering, resulting in a concomitant decrease in the terahertz reflectivity. In comparing the QCL detection system to the THz TDS system, the QCL system was more effective in detecting early onset of corrosion since the rust resulting from γ-FeO(OH) exhibits absorption peaks at around 6.6 THz and 9.3 THz whose tails spectrally overlap the frequency range of the QCL. The authors report that the absorption coefficient for 2.5 THz waves (QCL) is about 40 times higher as compared to the ~ 0.3 THz waves which are employed in THz-TDS thereby enabling detection using the QCL system of even small amounts of corrosion with corresponding relatively weak terahertz absorption.

In developing terahertz nondestructive evaluation to evaluate the degradation of multilayer paint stacks with aging, it is important to consider what aspects of the paint layer properties that are probed by terahertz waves might change with coating degradation. Clearly, if the dielectric paint layers are degraded, this might be manifested either in changing layer thicknesses or in the Debye model permittivity. In addition, chemical corrosion of a metallic substrate or layer, as discussed above, creates a rough surface that increasingly scatters terahertz radiation with corrosion. Changes in these parameters will alter not only the amplitudes but also the timings of the reflected pulses from each layer in the paint stack resulting in a change in the overall reflected THz-TD waveform as well as the deconvoluted waveform.

The reflectivity of a rough metallic surface can be modeled using the Beckmann and Spizzichino model (Beckmann and Spizzichino, 1987; Cacciari and Siano, 2017). Using this model, the mean power (i.e., square amplitude of electric field) in the specular reflected direction may be written as

$$P_s = e^{-g}\left(1 + \frac{\tau_L\sqrt{\pi}}{2D}\sum_{m=1}^{\infty}\frac{g^m}{m!\sqrt{m}}\right) \tag{41}$$

where

$$\sqrt{g} = 4\pi\frac{R_q v}{c_o}, \tag{42}$$

D is the terahertz beam spot size, R_q is the standard deviation of the normally distributed heights of the rough surface, τ_L is the correlation distance, c_o is the speed of light in a vacuum, and v is the terahertz frequency. When $R_q = 0$, corresponding to a flat metallic surface with no surface roughness, Eq. (41) reduces to unity indicating perfect reflection from a flat metal surface. When the surface roughness is present, the power in the specular reflected direction is reduced with increasing roughness since the rough surface scatters some of the terahertz power into non-specular directions. In the limit of small roughness $g \ll 1$, the power P_s can be shown to approximately depend quadratically on the terahertz frequency

$$P_s \simeq 1 - \left(\frac{4\pi R_q v}{c_o}\right)^2\left(1 - \frac{\tau_L\sqrt{\pi}}{2D}\right). \tag{43}$$

If the terahertz source is a broad-banded pulse source, such as with terahertz time-domain spectroscopy, the spot size D of the focused pulse depends on the terahertz frequency. Assuming a terahertz Gaussian beam with initial diameter D_f which is focused to a spot size D using a lens of focal length f, the spot size at the focus can be approximated as $D = c_o f/\pi D_f v$. In this case, the power P_s becomes

$$P_s \simeq 1 - \left(\frac{4\pi R_q v}{c_o}\right)^2\left(1 - \frac{\tau_L\pi^{3/2}D_f v}{2c_o f}\right). \tag{44}$$

Accelerated corrosion protocols

Many of the published studies of terahertz nondestructive evaluation of buried corrosion layers, such as those cited above, did not follow any established protocol for accelerated corrosion testing of samples. Their emphasis was to establish the prospect of terahertz NDE of buried corrosion. In the rest of this section, terahertz NDE of multilayer paint samples is described in which the samples were exposed to an accelerated corrosion test method (Dante, 2019). The samples are periodically removed from the accelerated corrosion chamber to characterize the corroded samples using terahertz NDE.

The accelerated corrosion methodology combines cycling of dry and wet environmental conditions with 'aggressive'—meaning higher salt concentration and higher acidity (pH < 5)—salt-fog solutions. For the work presented in this section, the accelerated corrosion test method of Dante (2019) was adopted. The core components of the corrosion solution are seawater as detailed in Table 2. As described by Dante, nitrate is added because all coastal sites from which they acquired chemical samples showed nitrate. Moreover, the nitrate solution is realistic since it is also an important oxidizer in atmospheric chemistry. The low pH is the result of sea salt aerosols (around 1 µm) exhibiting pH values of approximately 3. Due to the low pH in the solution, the saltwater solution is only applied via fog for 6 h twice a week. Subsequent to fog exposure, the relative humidity is cycled for either 3 or 4 days until the next salt fog exposure. The relative humidity cycling is performed at 40 °C; the samples spend 2 h at 90% RH 3 h at 65% RH and 1 h at 40% RH. This cycle repeats until the next fog exposure with a total of two fog exposures in a 1 week period.

The multilayer paint samples, illustrated in Fig. 17a consisted of an aluminum substrate, primer layer (approximately 0.7 mils thick), conductive layer (approximately 1.1 mils thick), a second primer layer, rain erosion layer (approximately 10 mils), and an ultraviolet blocking topcoat layer (approximately 1.7 mils). The tested coupons (roughly 3 in. by 3 in.), were cut from larger painted panels. These cuts made the edges of the samples vulnerable to the solution seeping in through the side of the sample as opposed to through the topcoat layer, so the edges of the samples were covered with waterproof tape.

On a weekly basis, just prior to exposure in the salt fog chamber, the multilayer paint samples are removed from the humidity chamber for THz-TD testing. Prior to testing, the samples are rinsed with deionized water and blown dry with air to remove any surface build-up of salt deposits. The surface salt deposits are removed so that their presence on the surface does not lead to any artifacts in the terahertz waveform due to scattering from the deposits. Experiments have shown that the subsequent 6 h exposure to salt fog will fully saturate the coating for the next humidity cycle. To eliminate potential contribution of water absorbed into the paint layers to the measured terahertz waveform, prior to terahertz characterization the samples are dried in a constant flow of 50 °C dry air for 1 h. Time-domain waveforms and images were acquired using a Terametrix T-Ray 5000 THz time-domain system.

Results

By measuring the amplitude of the reflected terahertz radiation within a fixed frequency band, one can easily generate images of the corrosion progression as shown in Fig. 16. The frequency-dependent reflectivity is calculated by dividing the reflected frequency-dependent magnitude by the frequency spectrum of a reference pulse which was reflected from a flat metal plate. The average reflectance within a specific frequency band is then calculated for each pixel. The upper left image is recorded from the sample prior to any accelerated corrosion. The darker gray lines near the boundary of the sample represent the edges of the tape on the samples. Note that prior to accelerated corrosion (upper left image) that the reflectivity of the sample is very uniform across the sample. As the sample undergoes accelerated corrosion, the reflectivity decreases near the corners and edges of the sample where the salt-fog is able (a) to penetrate through gaps in the tape or (b) effectively collect under the tape near the sample edges.

In addition to the time-domain analysis described above in which the permittivity of each layer is assumed to obey a Debye relaxation model (Eq. 32), the reflected terahertz waveform may also be analyzed using a deconvoluted pulse approach. In its simplest form, the deconvoluted pulses represent the partial reflection of terahertz radiation from each boundary in the multilayer paint stack. The deconvolution analysis enables one to determine the amplitude as well as the arrival time from each partial reflection. The advantage of this simplified approach compared to the time-domain analysis in Section "Terahertz NDE of multilayer paints" is that one does not need to assume any particular functional form (i.e., Debye relaxation model) for the paint layer permittivity.

A typical terahertz time-domain reflected waveform from an undegraded sample and the corresponding deconvoluted waveform which is calculated using the Tray 5000 software is shown in Fig. 17b. The deconvolution algorithm uses a reference wave-form which is acquired by replacing the sample with a flat metallic plate. The deconvolution waveform shows four main peaks. Peak 1 is the front reflection from the air-top coat boundary. Peak 2 is the reflection from the top coat/rain erosion boundary. Peak 3 is a reflection from the aluminum substrate. Peak 4 is due to multiple reflections between the front surface of the coating and the aluminum substrate. The refractive index of the rain erosion layer is similar to that of the thin primer layer such that there is no observable reflection from the rain erosion/primer boundary.

A simple analytical method to determine if the multilayer paint stack is changing with corrosion is to analyze the arrival times and amplitudes of the deconvoluted pulses. For this analysis method, assumptions of particular models for the dielectric layers (i.e., Debye) nor metallic substrate (e.g., Drude) are not required. As an example, the time delay between the deconvolved pulse 2 and 1 is a measure of the optical path length (i.e., real refractive index multiplied by the thickness) of the topcoat layer while the time delay

Table 2   Composition of modified sea salt solution for corrosion testing.

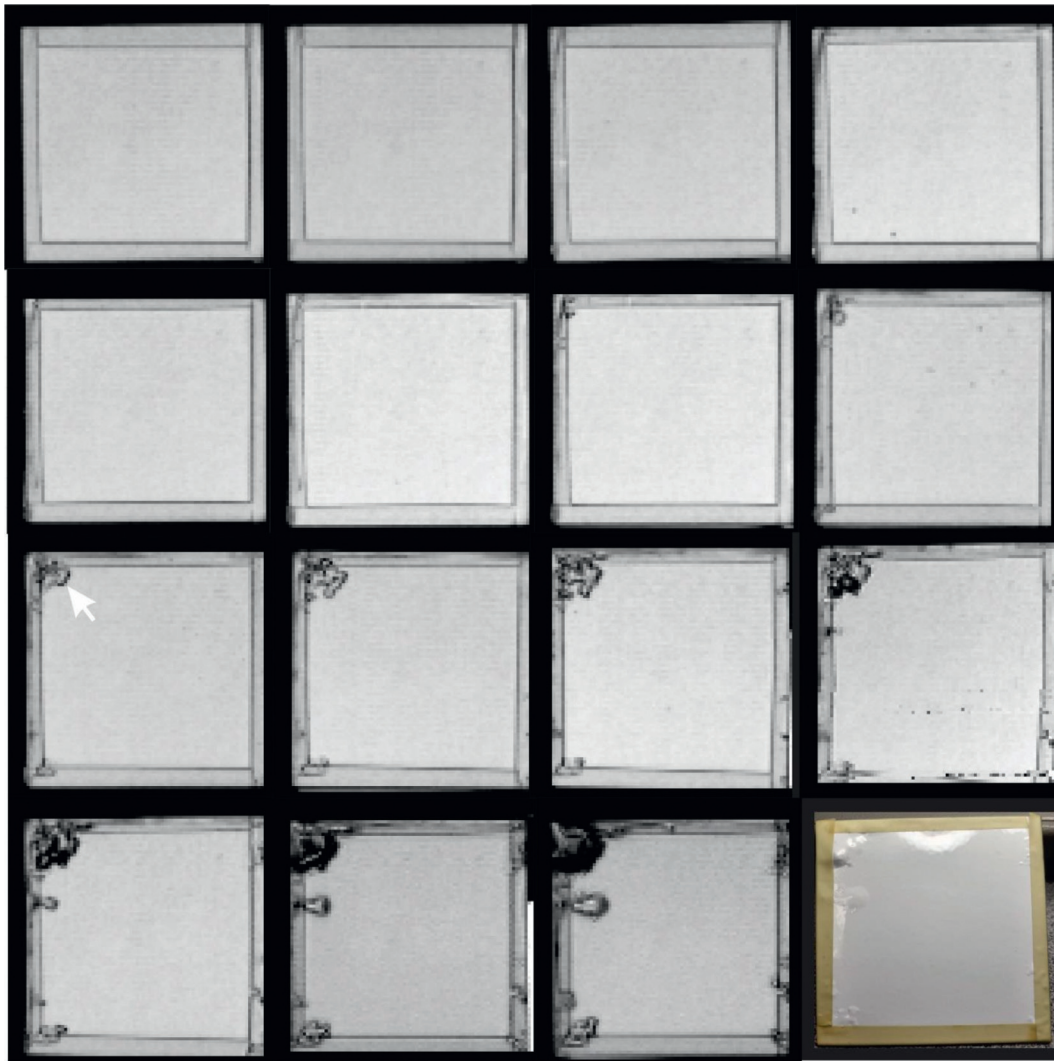| Modified Sea Salt Solution with Nitrate Ions	
NaCl	22.26 g L^{-1}
MgCl$_2$ • 6H$_2$O	11.10 g L^{-1}
Na$_2$SO$_4$	4.00 g L^{-1}
NaNO$_3$	3.27 g L^{-1}
HCl (1 N)	(1 mL)

Fig. 16   Time sequence of terahertz images taken at weekly intervals during accelerated aging. The images correspond to the average measured reflectivity of the terahertz waveform in the 0.5–1 THz range. Top left image was acquired prior to aging. The presence of tape on the edges of the sample is evident in the images as well as the onset of corrosion from the edges of the sample.
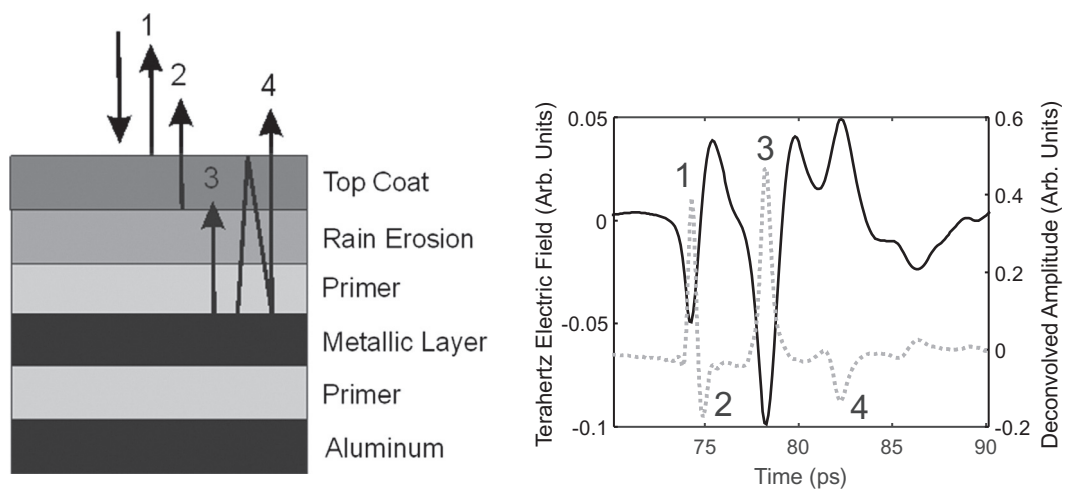

Fig. 17   (a) Schematic of multilayer paint samples. (b) Typical reflected terahertz waveform (solid black, left axis) and deconvoluted waveform (dashed gray, right axis) from center pixel location of the sample. Main peaks of the deconvolved waveform are labeled from 1 to 4.
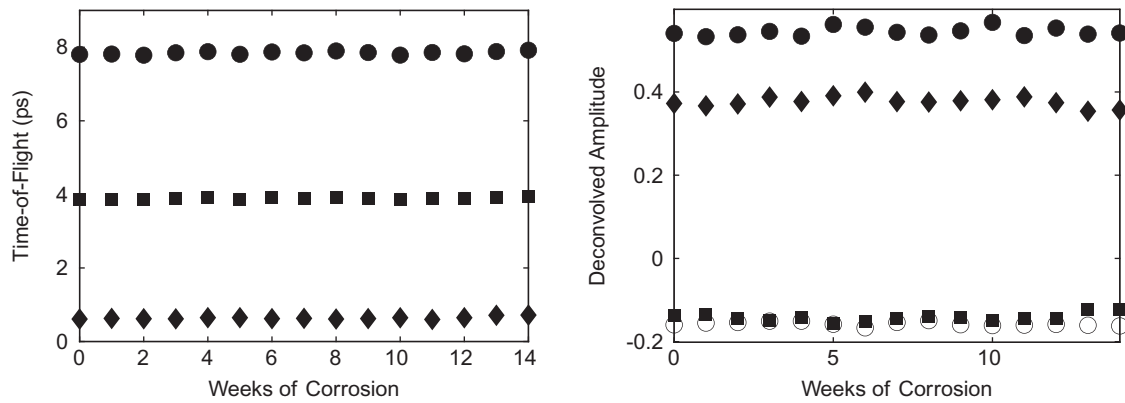
Fig. 18   (a) Measured time-of-flight between pulses 2 and 1 (diamond), 3 and 1 (square), and 4 and 1 (circle) as a function of number of weeks of corrosion. (b) Deconvolved amplitudes of pulses 1 (diamond), 2 (square), 3 (circle), and 4 (open circle) as a function of weeks of corrosion. Data is taken from a pixel at the center of the sample.

between pulse 3 and 2 is a measure of the optical path length of the rain erosion layer. Fig. 18a shows the measured time of flight between the various pulses as measured from the center of the sample. Note that the pulse time-of-flight relative to the front reflection from the center of the paint layer stack does not significantly change during the corrosion process. Likewise, the amplitudes of the various deconvoluted pulses (Fig. 18b) show essentially no change with accelerated corrosion. This suggests that the salt-fog corrosion degradation through the coating is a very slow process compared to corrosion through edges of the sample. Even after 14 weeks of degradation, the 'shine' of the topcoat layer as measured by visible light illumination is still present. Consequently, one may conclude that for the accelerated corrosion protocol used in this study, the Debye permittivity function and thicknesses of the dielectric layers are not degraded.

This result is consistent with the functioning of the UV-rain erosion layers. These layers are hydrophobic and tend to repulse the acidic salt fog. However, at the edges of the sample, the acidic salt fog is in contact with the metallic substrate under the paint layers. Consequently, the corrosion of the metallic layer through the edges of the sample is a much faster process than the comparably slow degradation through the UV-rain erosion layers.

The progress of the corrosion from the edges of the sample under the tape and inward towards the center of the sample is evidenced by the changing reflectance with increasing weeks of corrosion. The mechanism by which the reflectivity decreases is twofold: For the first step, the corrosion leads to an increase in roughness of the aluminum substrate which more efficiently scatters incident terahertz radiation. The second mechanism is a 'bulging' or 'blistering' of the multilayer paint stack as the corrosion continues and the paint layer stack detaches from the substrate. As shown in the visible image of the sample (bottom right panel of Fig. 16) after 14 weeks of corrosion, the chemical corrosion lifts the paint stack from the sample. Moreover, visible images of the edges of the sample confirm the failure of the primer layer and detachment of the rain erosion layer from the substrate surface.

After the edges of the sample corrode, the multilayer paint stack detaches from the substrate as shown by the visible images in Fig. 19. The topcoat appears white with a shiny finish. The thickest layer is the rain erosion layer which appears black in visible light. Visual inspection shows that for the triangular section of Fig. 19b for which the rain erosion layer (black in color) has completely detached from the substrate, the primer layers have failed: there are locations where no primer is still attached to the rain erosion layer. In other areas, the primer still remains attached to the rain erosion layer, but the bottom primer/metallic layers are no longer intact. Probing of the detached area with an ohmmeter indicates no electrical conductivity meaning that the metallic layer between the two primer layers has been rendered highly resistive.

By analyzing the arrival times and amplitudes of the deconvolved waveforms, one can observe the progression of the corrosion in time. Fig. 20 shows the measured amplitude of the deconvoluted pulse amplitudes as measured at the point indicated by the white arrow in Fig. 16. Prior to 7 weeks of degradation, the amplitudes of the pulses are essentially unchanged. However, in week 8 begins a reduction in the magnitude of all four pulses indicating the progression of corrosion to that point on the sample.

It is interesting to note that while the deconvoluted amplitudes show evidence of corrosion at 8 weeks, the time-of-flight measurements do not show any significant change until 12 weeks. The unchanging time-of-flight values indicate that the multilayer stack from the top coat/rain erosion layer/primer layer/metallic layer remains intact during the early stages of corrosion. Examination of the deconvoluted pulses suggests that the four peaks of Fig. 17b remain at fixed relative positions even as the substrate roughens during corrosion. In this scenario, the detachment of the paint layer primarily occurs at the primer/ substrate boundary.

While Fig. 16 clearly shows the progression of corrosion under the multilayer paint stack with aging, the regions of reduced terahertz reflectivity very closely follow regions of bulging which are readily apparent in the visible images. Does terahertz NDE reveal the presence of corrosion before the effects of the corrosion are visibly apparent on the surface? To answer this question, one needs to separate the two contrast mechanisms for detection of corrosion: (a) increased surface roughness of the metal due to chemical corrosion (b) followed by bulging of the surface due to detachment of the multilayer paint stack from the substrate. The roughening of the metallic layer precedes and ultimately causes the detachment of the multilayer paint stack from the substrate.
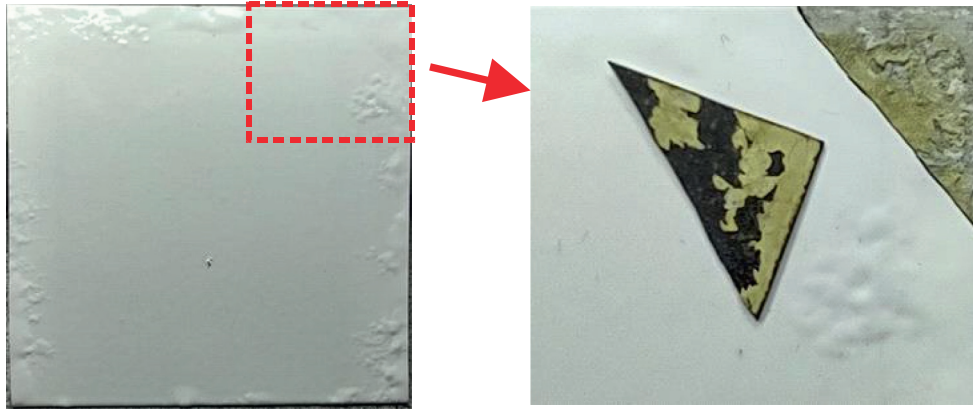
Fig. 19 Visible images of a corroded sample after 15 weeks. (a) top view of the corroded sample. (b) close up of the same sample with detached portion of coating cut away.
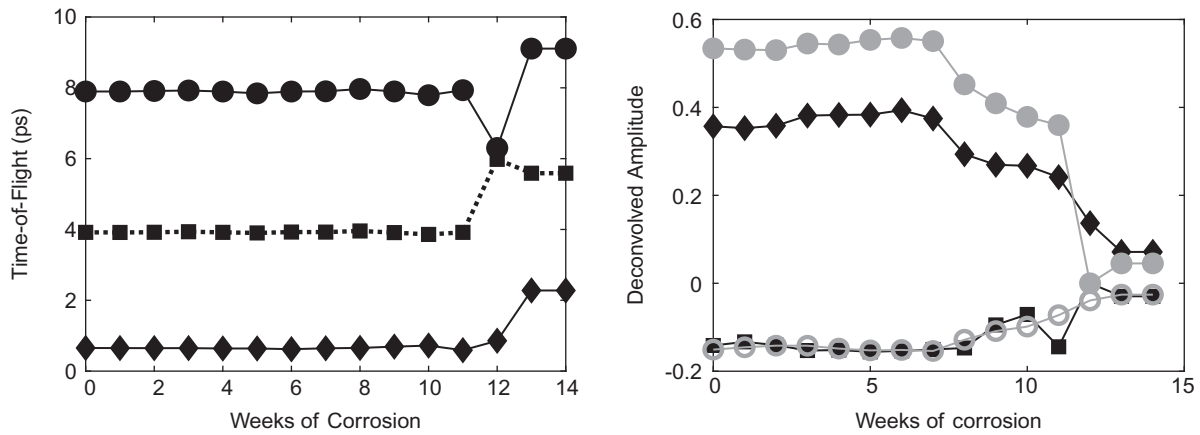

Fig. 20 Measured (a) pulse time-of-flight and (b) deconvolved amplitude at pixel (x = 15, y = 13). This pixel is denote by the white arrow. Notation for symbols is the same as Fig. 18.

The bulging leads to a reduction in the detected reflected terahertz power since the tilt of the bulging surface directs some terahertz power away from the terahertz receiver.

The topology (and bulging) of the front surface of the paint stack can be extracted from the terahertz data by plotting the arrival time of the deconvolved pulse from the front surface reflection (i.e., air-top coat boundary) of the paint stack. The local height of the bulge can be calculated by measuring the time difference of pulse Δt reflected from a region of the sample where no bulge is present and a location where the bulge is present. The height of the bulge is simply given by $c_o \Delta t / 2$.

Fig. 21a shows a higher resolution (0.2 mm pixel size) reflectivity image of a small portion of the sample after 15 weeks of corrosion. A horizontal slice of data, as indicated by the black line, is analyzed to extract the surface height and Peak 3 amplitude. The dashed line in Fig. 21b indicates the location where the surface height begins to increase indicating the edge of the bulging blister as the pixel position moves from right to left towards the bulging paint surface. At larger pixel positions ($\sim$72–80), the bulging is proceeded by a reduction in the peak 3 amplitude as a result of increased surface roughness due to corrosion. A measurable reduction with accelerated corrosion in the amplitude of the 3rd deconvolved pulse from the metallic layer may be an early indicator that the entire stack will soon detach from the substrate creating a bulge (i.e., blister) on the surface.

Regions of increased substrate roughness due to corrosion may also be visualized using polarized light reflection. Monte Carlo modeling of terahertz propagation and reflection from rough surfaces (Xie et al., 2022) show that roughening of the metallic surface leads to a randomization of the polarization direction of the reflected radiation. As an example, (Xie et al., 2022) shows significant cross-polarization scattering for radiation with a terahertz wavelength of 0.3 mm when the RMS surface roughness R_s becomes 0.5 mm and the correlation length τ decreases to 5 mm. The T-Ray 5000 transmitter and receiver modules are polarization sensitive. Cross-polarization images are acquired by orienting the polarization axes of the transmitter and receiver modules so that they are orthogonal. With this cross-polarization orientation, only reflected radiation that has been scattered into the cross-polarization orientation will be detected. Fig. 22 highlights areas of the sample which surround the bulge in the paint layers. The area immediately surrounding the bulge represents regions of the metallic layer which has been roughened by corrosion.
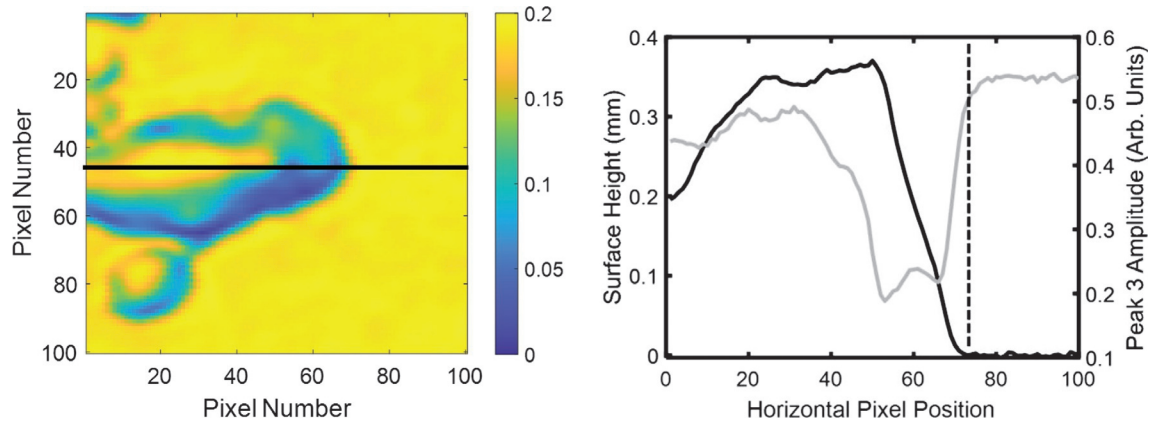
Fig. 21   (a) High resolution Terahertz reflectivity image (arbitrary units) in the 0.5–1 THz frequency band of a 20 mm by 20 mm section of sample showing a bulging blister on the paint layer surface. (b) The surface height and peak 3 amplitude as measured along a horizontal slice as indicated by the black horizontal line in (a). The dashed line indicates the location where the surface height begins to increase indicating the edge of the bulging blister. At higher pixel positions, the bulging is preceded by a reduction in the peak 3 amplitude as a result of increased surface roughness due to corrosion.
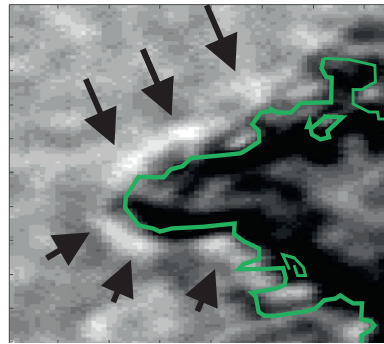

Fig. 22   Cross polarization image (0.2 mm pixel size) measuring total power (unnormalized) in 0.5–1 THz band. Green outline indicates boundary—as determined by the time arrival of the front surface reflection (pulse 1) from the paint layer stack—that is bulging at least 30 μm. Brighter portions of the image surrounding edge of bulge (indicated by black arrows) indicate regions of enhanced scattering due to surface roughness from corrosion.

Conclusion

In its current strategy, the DoD defines the number one barrier to moving AM into the realm of accepted manufacturing technologies as "rapid and standardized approaches for qualification of materials and processes, and certification of AM parts." Terahertz nondestructive evaluation techniques could play a major role in the creation of a standardized qualification process for additively manufactured components. This chapter has showcased the current use of THz NDE on two emerging material applications: additively manufactured components and multilayer paint stacks. For the first application, NDE of fused deposition modeling (FDM) printed plastics and nanoparticle jetted ceramics were emphasized. These examples represent an initial utilization of this technology for AM. As new materials for AM are developed and new printing techniques are created, the requirement to standardize approaches for rapid qualification of materials and processes will be unchanged. THz NDE can and should be applied to aid in the maturing process of this technology, whether it is using it for defect detection, creating full 3D reconstructions, or measuring a material's electromagnetic properties as just a few prime examples.

Aside from terahertz optical components, THz NDE of additively manufactured components can detect defects in the 3D printed structures which could significantly impact their functionality. Simple examples include cracks/voids in the printed structure and regions of high mechanical stress. A complete 3D image of an AM part could enable detailed comparison of design versus printed dimensions, structural defects, etc. THz CT of AM parts has many of the same analysis capabilities as X-ray CT: detection of internal voids and defects, measure internal and external geometry, and ability to compare printed parts to their CAD design. A significant challenge to the implementation of THz CT is refraction of the THz rays by the sample. Corrections to THz CT analysis to account for Gaussian beam propagation as well as refractive effects (using SART, ART, etc.) have been demonstrated.

Owing to refractive effects, THz NDE is best suited to planar structures. Examples include the material characterization and thickness measurements of multilayer paint stacks. Adapting THz NDE to corrosion detection shows that the methodology has sufficient sensitivity for early detection of failures due to corrosion in multilayer paint structures. Based on the accelerated corrosion

studies using salt-fog exposure and humidity cycling, a 5.6% change in the reflectivity from the metallic layer indicates significant chemical corrosion of the multilayer paint coating prior to any visible evidence of a blister on the coating surface. Further chemical corrosion (and commensurate decrease in terahertz reflectivity) leads to detachment of the coating from the substrate.

The major driving force behind the development of additively manufactured terahertz and microwave components is the development of next-generation wireless communication systems. Some of the currently used polymers for the manufacturing of terahertz optical components include high-density polyethylene (HDPE), polypropylene, polystyrene, and TOPAS. Most of these polymers exhibit relatively minimal attenuation, but also have refractive indices close to 1.5. Several research teams have succeeded in creating by 3D printing various THz quasi-optical devices including GRIN lenses, topological waveplates, phase plates, polarization splitters, q-plates, and stepped-refractive-index lenses.

Acknowledgments

References

Abraham E, Younus A, Aguerre C, Desbarats P, and Mounaix P (2010) Refraction losses in terahertz computed tomography. *Optics Communications* 283: 2050–2055.

Alfattni R (2022) Comprehensive Study on Materials used in Different Types of Additive Manufacturing and their Applications. *International Journal of Mathematical, Engineering and Management Sciences* 7: 92–114.

Anastasi RF, Madaras EI, Seebo JP, Smith SW, Lomness JK, Hintze PE, Kammerer CC, Winfree WP, and Russell RW (2007) Terahertz NDE Application for Corrosion Detection and Evaluation under Shuttle Tiles. *Proceedings of SPIE* 6531: 65310W.

Beckmann P and Spizzichino A (1987) *The Scattering of Electromagnetic Waves from Rough Surfaces*. Norwood, Artech House.

Bohn M and Petkie D (2013) Terahertz applications in the aerospace industry. In: Saeedkia D (ed.) *Handbook of Terahertz Technology for Imaging, Sensing, and Communications*. Philadelphia: Woodhead Publishing.

Burger R, Frisch J, Hübner M, Goldammer M, Peters O, Rönneberg E, and Wu D (2021) Thz-tds reflection measurement of coating thicknesses at non-perpendicular incidence: Experiment and simulation. *Sensors* 21: 3473.

Busboom I, Nguyen TT, Christmann S, Feige VKS, Haehnel H, and Tibken B (2021) Terahertz Imaging of 3D Print Infill Structures. In: *15th European Conference on Antennas and Propagation*, EuCAP 2021.

Cacciari I and Siano S (2017) Use of THz Reflectometry for Roughness Estimations of Archeological Metal Surfaces. *Journal of Infrared, Millimeter, and Terahertz Waves* 38: 503–517.

Castro-Camus E, Koch M, and Hernandez-Serrano AI (2020) Additive manufacture of photonic components for the terahertz band. *Journal of Applied Physics* 127: 210901.

Catapano I, Soldovieri F, Mazzola L, and Toscano C (2017) THz Imaging as a Method to Detect Defects of Aeronautical Coatings. *Journal of Infrared, Millimeter, and Terahertz Waves* 38: 1264–1277.

Chan WL, Deibel J, and Mittleman DM (2007) Imaging with terahertz radiation. *Reports on Progress in Physics* 70: 1325–1379.

Clark AT (2022) *Nondestructive Evaluation of 3D Printed, Extruded and Natural Polymer Structures using Terahertz Spectroscopy and Imaging*. Ph.D. Doctoral Dissertation, New Jersey Institute of Technology.

Clark AT, Federici JF, and Gatley I (2021) Effect of 3D Printing Parameters on the Refractive Index, Attenuation Coefficient, and Birefringence of Plastics in Terahertz Range. *Advances in Materials Science and Engineering* 2021: 8276378.

Dally JW (1978) *Experimental Stress Analysis*, 3rd edn. McGraw-Hill.

Dante JF (2019) *Cyclic Corrosion and Failure Mechanisms*. Available: https://www.serdp-estcp.org/Tools-and-Training/Webinar-Series/04-25-2019/Webinar-88-Slides.

Dhawan AP (2003) *Medical Image Analysis*. Hoboken, NJ: John Wiley & Sons.

Dhawan AP, Huang HK, and Dim D-S (2008) *Principles and Advanced Methods in Medical Imaging and Image Analysis*. New Jersey: World Scientific.

Dong J, Locquet A, and Citrin DS (2017) Terahertz quantitative nondestructive evaluation of failure modes in polymer-coated steel. *IEEE Journal on Selected Topics in Quantum Electronics* 23.

Ellrich F, Bauer M, Schreiner N, Keil A, Pfeiffer T, Klier J, Weber S, Jonuscheit J, Friederich F, and Molter D (2020) Terahertz Quality Inspection for Automotive and Aviation Industries. *Journal of Infrared, Millimeter, and Terahertz Waves* 41: 470–489.

Evans B (2012) *Practical 3D Printers: The Science and Art of 3D Printing*. Netherlands: Apress.

Federici JF (2012) Review of Moisture and Liquid Detection and Mapping using Terahertz Spectroscopy and Imaging. *IEEE Transactions on Terahertz Science and Technology* 33: 97–126.

Federici J and Moeller L (2010) Review of terahertz and subterahertz wireless communications. *Journal of Applied Physics* 107: 111101.

Federici J, Moeller L, and Su K (2013) Terahertz communication. In: Saeedkia D (ed.) *Handbook of Terahertz Technology for Imaging, Sensing, and Communications*. Cambridge: Woodhead Publishing.

Federici JF, Ma J, and Moeller L (2016) Review of Weather Impact on Outdoor Terahertz Wireless Communication Links. *Nano Communication Networks* 10: 13–26.

Ferguson B, Wang S, Gray D, Abbott D, and Zhang X-C (2002) Towards functional 3D T-ray imaging. *Physics in Medicine and Biology* 47: 3735–3742.

Fielding J, Davis A, Bouffard B, Kinsella M, Delgado T, Wilczynski J, Marchese K, and Wing I (2021) *Final Report - Department of Defense Additive Manufacturing Roadmap*. Washington, DC: Department of Defense. Available: https://www.americamakes.us/wp-content/uploads/2021/10/Final-Report-DoDRoadmapping-FINAL120216.pdf.

Fosodeder P, Hubmer S, Ploier A, Ramlau R, van Frank S, and Rankl C (2021) Phase-contrast THz-CT for non-destructive testing. *Optics Express* 29: 15711–15723.

Fukuchi T, Fuse N, Mizuno M, and Fukunaga K (2013) THz measurement of refractive index and thickness of ceramic coating on a metal substrate. In: *Pacific Rim Conference on Lasers and Electro-Optics, CLEO - Technical Digest*.

Furlan WD, Ferrando V, Monsoriu JA, Zagrajek P, Czerwińska E, and Szustakowski M (2016) 3D printed diffractive terahertz lenses. *Optics Letters* 41: 1748–1751.

Fuse N, Fukuchi T, Takahashi T, Mizuno M, and Fukunaga K (2012) Evaluation of applicability of noncontact analysis methods to detect rust regions in coated steel plates. *IEEE Transactions on Terahertz Science and Technology* 2: 242–249.

Fuse N, Fukuchi T, Mizuno M, and Fukunaga K (2016) High-speed underfilm corrosion imaging using a terahertz camera. *Electronics and Communications in Japan* 99: 86–92.

Goulas A, Chi-Tangyie G, Wang D, Zhang S, Ketharam A, Vaidhyanathan B, Reaney IM, Cadman DA, Whittow WG, Vardaxoglou JYC, and Engstrøm DS (2020) Microstructure and microwave dielectric properties of 3D printed low loss $Bi_2Mo_2O_9$ ceramics for LTTC applications. *Applied Materials Today* 21: 100862.

Hecht E (2017) *Optics*, 5th edn. Pearson Education Limited.

Joint Defense Manufacturing Council (2021) *Department of Defense Additive Manufacturing Strategy*. Washington, DC: Office of the Under Secretary of Defense for Research and Engineering. Available: https://www.cto.mil/wp-content/uploads/2021/01/dod-additive-manufacturing-strategy.pdf.

Kang K, Du Y, Wang S, An Li L, Wang Z, and Li C (2021) Full-field stress measuring method based on terahertz time-domain spectroscopy. *Optics Express* 29: 40205–40213.

Kim H, Kim KW, Park J, Han JK, and Son JH (2012) Terahertz tomographic imaging of topical drugs. In: *2012 Conference on Lasers and Electro-Optics, CLEO*.

Krimi S, Klier J, Jonuscheit J, Von Freymann G, Urbansky R, and Beigang R (2016) Highly accurate thickness measurement of multi-layered automotive paints using terahertz technology. *Applied Physics Letters* 109: 021105.

Krimi S, Torosyan G, and Beigang R (2017) Advanced GPU-Based Terahertz Approach for In-Line Multilayer Thickness Measurements. *IEEE Journal of Selected Topics in Quantum Electronics* 23.

Lee AWM, Kao TY, Burghoff D, Hu Q, and Reno JL (2012) Terahertz tomography using quantum-cascade lasers. *Optics Letters* 37: 217–219.

Li Q, Li YD, Ding SH, and Wang Q (2012) Terahertz computed tomography using a continuous-wave gas laser. *Journal of Infrared, Millimeter, and Terahertz Waves* 33: 548–558.

Markl D, Zeitler JA, Rasch C, Michaelsen MH, Müllertz A, Rantanen J, Rades T, and Bøtker J (2017) Analysis of 3D prints by X-ray computed microtomography and terahertz pulsed imaging. *Pharmaceutical Research* 34: 1037–1052.

Mittleman D (2003) *Sensing With Terahertz Radiation*. Springer.

Mittleman DM, Hunsche S, Boivin L, and Nuss MC (1997) T-ray tomography. *Optics Letters* 22: 904–906.

Morales CD, Morlaas C, Chabory A, Pascaud R, Grzeskowiak M, and Mazingue G (2021) 3D-printed ceramics with engineered anisotropy for dielectric resonator antenna applications. *Electronics Letters* 57: 679–681.

Moylan, S. (n.d.) *Qualification for Additive Manufacturing Materials, Processes, and Parts*. Gaithersburg, MD: NIST. Available: https://www.nist.gov/programs-projects/qualification-additive-manufacturing-materials-processes-and-parts.

Mukherjee S, Federici J, Lopes P, and Cabral M (2013) Elimination of fresnel reflection boundary effects and beam steering in pulsed terahertz computed tomography. *Journal of Infrared, Millimeter, and Terahertz Waves* 34: 539–555.

Naftaly M, Tikhomirov I, Hou P, and Markl D (2020) Measuring open porosity of porous materials using thz-tds and an index-matching medium. *Sensors (Switzerland)* 20.

Nishina S, Takeuchi K, Shinohara M, Imamura M, Shibata M, Hashimoto Y, and Watanabe F (2012) Novel nondestructive imaging analysis for catalyst washcoat loading and DPF soot distribution using terahertz wave computed tomography. *SAE International Journal of Fuels and Lubricants* 5: 343–351.

Perraud JB, Obaton AF, Bou-Sleiman J, Recur B, Balacey H, Darracq F, Guillet JP, and Mounaix P (2016) Terahertz imaging and tomography as efficient instruments for testing polymer additive manufacturing objects. *Applied Optics* 55: 3462–3467.

Posodeder P, Frank SV, and Rankl C (2022) Highly accurate THz-CT including refraction effects. *Optics Express* 30: 3684–3699.

Prabhu SS (2018) Terahertz Spectroscopy: Advances and Applications. In: *Molecular and Laser Spectroscopy: Advances and Applications*. Elsevier.

Recur B, Younus A, Salort S, Mounaix P, Chassagne B, Desbarats P, Caumes JP, and Abraham E (2011) Investigation on reconstruction methods applied to 3D terahertz computed tomography. *Optics Express* 19: 5105–5117.

Rohrbach D, Kang BJ, and Feurer T (2021) 3D-printed THz wave- and phaseplates. *Optics Express* 29: 27160–27170.

Ruan X and Chan CH (2019) Terahertz free-space dielectric property measurements using time- and frequency-domain setups. *International Journal of RF and Microwave Computer-Aided Engineering* 29.

Saleh BEA and Teich MC (1991) *Fundamentals of Photonics*. New York: John Wiley & Sons.

Sathishkumar N, Udayakumar ASM, Vincent B, and Kumar VA (2020) Study and analysis of 3D printed FDM components by non-destructive testing techniques. *International Journal of Research and Review* 5: 6.

Serrano AIH (2018) *Terahertz Quasi-Optical Devices Fabricated by 3D Printing*. PhD, León, Guanajuato, México.

Siemion A, Melaniuk A, Zagrajek P, Komorowski P, Walczakowski M, Surma M, Sobotka P, Ducin I, and Czerwinska E (2020) THz diffractive lens manufactured using 3D printer working for 0.6 THz. In: *2020 23rd International Microwave and Radar Conference, MIKON 2020*, pp. 225–228.

Stoik CD, Bohn MJ, and Blackshire JL (2008) Nondestructive evaluation of aircraft composites using transmissive terahertz time domain spectroscopy. *Optics Express* 16: 17039–17051.

Su K, Shen Y, and Zeitler JA (2014) Terahertz Sensor for Non-Contact Thickness and Quality Measurement of Automobile Paints of Varying Complexity. *IEEE Transactions on Terahertz Science and Technology* 4: 432–439.

Takeshi Yasui TY, Sawanaka KI, and Araki T (2005) Terahertz paintmeter for noncontact monitoring of thickness and drying progress in paint film. *Applied Optics* 44: 6849–6856.

Taubmann O, Berger M, Bögel M, Xia Y, Balda M, and Maier A (2018) Computed tomography. In: Maier A, Steidl S, Christlein V, and Hornegger J (eds.) *Medical Imaging Systems: An Introductory Guide*. Cham: Springer.

Tepe J, Schuster T, and Littau B (2017) A modified algebraic reconstruction technique taking refraction into account with an application in terahertz tomography. *Inverse Problems in Science and Engineering* 25: 1448–1473.

Tu W, Zhong S, Luo M, and Zhang Q (2021) Non-destructive evaluation of hidden defects beneath the multilayer organic protective coatings based on terahertz technology. *Frontiers in Physics* 9: 676851.

van Mechelen JLM, Kuzmenko AB, and Merbold H (2014) Stratified dispersive model for material characterization using terahertz time-domain spectroscopy. *Optics Letters* 39: 3853–3856.

Waddie AJ, Schemmel PJ, Chalk C, Isern L, Nicholls JR, and Moore AJ (2020) Terahertz optical thickness and birefringence measurement for thermal barrier coating defect location. *Optics Express* 28: 31535–31552.

Wang S and Zhang X-C (2004) Pulsed terahertz tomography. *Journal of Physics D: Applied Physics* 37: R1–R36.

Wang D, Ning R, Li G, Zhao J, Wang Y, and Rong L (2022) 3d image reconstruction of terahertz computed tomography at sparse angles by total variation minimization. *Applied Optics* 61: B1–B7.

Xie P, Guan K, He D, Yi H, Dou J, and Zhong Z (2022) Terahertz Wave Propagation Characteristics on Rough Surfaces Based on Full-Wave Simulations. *Radio Science* 57. e2021RS007385.

Yasuda H and Hosako I (2008) Measurement of terahertz refractive index of metal with terahertz time-domain spectroscopy. *Japanese Journal of Applied Physics* 47: 1632–1634.

Yasuda T, Yasui T, Araki T, and Abraham E (2006) Real-time two-dimensional terahertz tomography of moving objects. *Optics Communications* 267: 128–136.

Yasuda T, Iwata T, Araki T, and Yasui T (2007) Improvement of minimum paint film thickness for THz paint meters by multiple-regression analysis. *Applied Optics* 46: 7518–7526.

Yilmaz T and Akan OB (2020) Attenuation constant measurements of clear glass samples at the low terahertz band. *Electronics Letters* 56: 1423–1425.

Zhang X-C (2003) Three-dimensional terahertz wave imaging. *Philosophical Transactions of the Royal Society A* 362: 283–299.

Zhang B, Chen W, Wu Y, Ding K, and Li R (2017) Review of 3D printed millimeter-wave and terahertz passive devices. *International Journal of Antennas and Propagation* 2017: 1297931.

Zhao M, Geng Y, Fan S, Yao X, Zhu M, and Zhang Y (2021) 3D-printed strong hybrid materials with low shrinkage for dental restoration. *Composites Science and Technology* 213: 108902.